Journal of Materials Chemistry C

B-Site Doped Lead Halide Perovskites: Synthesis, Band Engineering, Photophysics, and Light Emission Applications

Journal:	*Journal of Materials Chemistry C*
Manuscript ID	TC-REV-11-2018-005741.R1
Article Type:	Review Article
Date Submitted by the Author:	17-Jan-2019
Complete List of Authors:	Luo, Binbin; Shantou University Li, Fei; University of Science and Technology Beijing Xu, Ke; Chongqing University Guo, Yan; Shantou University Liu, Ying; University of Science and Technology Beijing, School of Materials Science and Engineering Xia, Zhiguo; University of Science and Technology Beijing, School of Materials Science and Engineering Zhang, Jin Zhong; University of California, Santa Cruz, Department of Chemistry & Biochemistry

B-Site Doped Lead Halide Perovskites: Synthesis, Band Engineering, Photophysics, and Light Emission Applications

Binbin Luo,[†,] Fei Li, [#] Ke Xu,[‡] Yan Guo[†], Ying Liu,[#] Zhiguo Xia[#] and Jin Z. Zhang[‡,*]*

† Department of Chemistry, Shantou University, Shantou, Guangdong 515063, China

‡ Department of Chemistry and Biochemistry, University of California, Santa Cruz, California 95064, United States

 # The Beijing Municipal Key Laboratory of New Energy Materials and Technologies School of Materials Sciences and Engineering, University of Science and Technology Beijing, Beijing 100083, China

Abstract: Lead halide perovskite (LHP) semiconductor with the general chemical formula ABX_3 has now been widely investigated for a variety of applications including but not limited to high-efficiency photovoltaics (PVs) and light-emitting diodes (LEDs). Introducing impurity atoms into the LHPs host through doping imparts new and interesting magnetic, electronic, and optical properties. Recent studies of doped LHPs have demonstrated great potential for their optoelectronic applications. In this review, we focus on the recent progress in the B-site doped LHPs including isovalent metal ions such as alkaline-earth metal ions (Ba^{2+}, Sr^{2+}), transition metal ions (Mn^{2+}, Zn^{2+}, Cd^{2+}, Ni^{2+}), and heterovalent metal ions exemplified by rare earth ions, Al^{3+}, Fe^{3+} and Bi^{3+}. In particular, electronic band engineering and electron/energy transfer processes in relation to doping are discussed in detail. We also highlight light emission applications of doped LHPs that take advantage of their strongly luminescent properties. Finally, we briefly discuss some remaining challenges and possible future directions for further research and development.

1. INTRODUCTION

The term "perovskite" was first used for $CaTiO_3$, which was discovered by the German mineralogist Gustav Rose in 1839 and named after Russian mineralogist Lev Perovski.[1, 2] This nomenclature now denotes a variety of compounds with same type of crystal structure as $CaTiO_3$ and general chemical formula ABX_3, in which B-site cation is coordinated by six X-site anions to form a $[BX_6]^{4-}$ octahedron and A-site cation is implanted in the void surrounding by eight corner-shared $[BX_6]^{4-}$ octahedra. Due to the large tunability of structure, a wide variety of transition metal ions, rare earth ions or alkaline earth metal ions have been incorporated into the lattice of ABO_3 perovskite oxides to improve the oxygen ionic conductivity, electronic conductivity, and catalytic activity, aiming at applications such as oxygen separation, solid oxide fuel cells, and catalytic conversions.[3-6]

Triggered by the fast development of $CH_3NH_3PbI_3$ on photovoltaics (PV) beginning in 2009,[7] lead halide perovskites (LHPs), including all inorganic elements exemplified by $CsPbX_3$ (X stands for halogen ion) and hybrid organic-inorganic composition such as $MAPbX_3$ (MA: $CH_3NH_3^+$) and $FAPbX_3$ (FA: $HC(NH_2)_2^+$), have been applied for diverse optoelectronic applications due to their unique properties including high absorption coefficient, photoluminescence (PL) quantum yield (QY), and defect-tolerance, as well as broad structure and bandgap tunability.[8-12] As a simple and powerful approach to manipulating the electronic, optical and magnetic properties, doping is widely used to introduce atoms/ions into host lattices to yield desirable properties and functionalities for

the targeted materials.[13] For semiconductor materials, doping usually create dopant-related energy levels within the interband region of host. The photo-induced excitons in the host can then transfer their energy to such bandgap states, often resulting in light emission characteristic of the dopant. For example, intensive orange PL (~ 600 nm) with lifetime up to 2 ms can be observed in Mn^{2+} doped II−VI nanocrystal (NC) systems due to the spin-forbidden nature of Mn^{2+}.[14] The electrical conductivity and type of dominate carriers can also be tailored by introducing heterovalent ions exemplified by B-doped Si (p-type) and N-doped Si (n-type).[15]

LHPs, as a new class of semiconductor materials and with a wide range of possible structures and bandgap tunability, provide an excellent platform for fundamental research on doping.[11, 16] Given the ternary composition of LHPs, the doping and alloying of LHPs have explored the replacement of all three sites: A, B and X. Since the A-site cation occupies the cage surrounding by the $[PbX_6]^{4-}$ octahedra, its size has a great impact on the structure distortion and stability according to the Goldschmidt's tolerance factor $\tau = \frac{R_A + R_X}{\sqrt{2}(R_B + R_X)}$, where R_A, R_B and R_X are the ionic radii for corresponding ions, respectively.[12] For most known 3D perovskites, $0.8 \leq \tau \leq 1.0$ is known as the empirical stability range, indicating the limit on R_A in LHPs is around 2.6 Å if using $\tau = 1.0$ and the largest values for R_B (R_{Pb} = 1.19 Å) and R_X (R_I = 2.20 Å).[12] To date, Cs^+ (1.67 Å), Rb^+ (1.52 Å), MA^+ (2.17 Å) and FA^+ (2.53 Å) cations can be utilized to construct 3D compounds.[12, 17] Due to the small radius of Cs^+, cubic α-$CsPbI_3$, which is suitable for diverse optoelectronic applications, shows poor stability at room temperature.[18, 19] Therefore, two or three cations

are usually mixed to enhance the stability.[20] X-site is usually the halogen ion, including Cl^-, Br^- and I^-. Due to the major contribution to the energy bands from the outmost p orbits of halogen ions, the bandgap of LHPs can be easily tuned across the entire visible range using mixed halides.[21] Besides the halide ions, pseudohalogen ion SCN^- was used for partially substituted LHPs, aiming for enhancing the moisture stability, controlling the crystal grain size, and tuning the optical properties based on the strong interaction between Pb^{2+} and the pseudohalogen ion.[22-26]

Doping of the B-site (*i.e.* Pb^{2+}) is more difficult compared to that of the A and X-sites owing to its large formation energy.[27] Also, complete substitution of Pb^{2+} often deteriorates the impressive optoelectronic properties of LHPs. Therefore, doping of the B-site is relatively less studied compared to that of the other two sites. As a member of the same group of Pb, Sn was first considered for replacing Pb in consideration of the high toxicity of Pb. However, the oxidation of Sn^{2+} to Sn^{4+} greatly hinders its development.[28] Two detailed studies of Mn^{2+}-doped LHPs reported in 2016 indicate that LHPs can function as the II−VI semiconductors, where the Mn^{2+} was doped into the B-site.[29, 30] Likewise, other dopants including transition ions and rare earth ions have been successfully doped into the B-site to tailor the optoelectronic properties of LHPs.[31, 32]

During the preparation of this paper, a review about metal-doped LHPs was published with a focus on optical properties and optoelectronic applications.[33] In this review, we will pay close attention to the photophysics and electronic band structure of B-site doped LHPs to understand the origin of charge and energy transfer between host and dopants. In

addition, the synthetic routes for doping with isovalent and heterovalent metal ions and the future applications on light emission are emphasized.

2. SYNTHESIS STRATEGIES

Doping metal ions into semiconductor NCs or quantum dots (QDs) has been extensively studied over the last two decades.[34, 35] Typically, dopants are implanted into the lattice during the crystal growth of the host or via ion exchange post host crystal growth.[36] Owing to the difference in atomic radii and charge number, dopants always induce lattice strain and defects, which may lead to the expulsion to the surface.[34] Therefore, doping in NCs is more difficult than in bulk due to the stronger strain and more defects of NCs. This suggests the particular need to develop synthesis strategies to prompt doping of NCs .[36]

2.1 One-pot hot injection

Hot-injection method is widely adopted to obtain Cs-based LHP NCs with well-defined morphology and controlled length, which was first reported by Kovalenko *et al*..[37] In terms of B-site doped LHP NCs, dopant precursors (usually metal halides) are firstly added into octadecene and dissolved with the help of carboxylic and amino ligands. However, the doping efficiency is much lower than anticipated in most situations due to the mismatch of size and/or charge.[29, 30, 38-40] Increasing dopants content and reaction temperature are effective in obtaining heavily doped LHPs.[41] For instance, doped $CsPbCl_3$ NCs with up to 46 at.% Mn^{2+} were obtained by adopting a high Mn:Pb ratio (10:1) and temperature (210 ℃).[42] The crystallinity of the host becomes worse with more dopants introduced,

which affects the process of energy transfer between host lattice and dopants.[42, 43] Compared to bulk materials, the strong lattice strain of NCs makes doping harder, especially for heavy doping. However, the large surface-to-volume-ratio of NCs also provides more opportunities for dopants to be involved in replacing Pb sites of lattice. Alkylamine hydrochloride has been demonstrated to control the size and increase the number of NCs, which promotes Mn^{2+} substitution for Pb sites.[14] With respect to other synthesis methods, hot injection creates a local high-temperature and inert atmosphere, which is helpful for many difficult doping reactions. For LHPs, many isovalent and aliovalent metal ions including (Al^{3+}, Bi^{3+}, Sn^{4+}, Ni^{2+} and some lanthanide ions) can be effectively single-doped or co-doped to tune their optical and magnetic properties using this method.[31, 39, 40, 44-48]

2.2 Ligand-assisted reprecipitation (LARP)

LARP was firstly proposed by Zhong and his colleagues in 2015 for synthesizing organic-inorganic LHPs.[21] The basic procedures include two main steps. First, a precursor solution is prepared by dissolving MA^+/Cs^+/FA^+, Pb^{2+} and halogen ion precursors and capping ligands (alkylamine and carboxylic acid) in polar solvents such as dimethylformamide (DMF) or dimethyl sulphoxide (DMSO). Second, the precursor solution is injected into antisolvents such as acetone/toluene/hexane under vigorous stirring. Compared to the hot-injection method, the reaction conditions of LARP are mild and easier to control. However, the obtained LHP NCs are usually damaged or dissolved to some degree during purification due to their high sensitivity to polar solvents. B-site doped LHP

NCs are most often obtained through injecting the dopant containing precursor solution into antisolvents or vice versa. By controlling the species of precursors and capping ligands, doped NCs with low dimensionalities can be synthesized.[38, 49, 50]

2.3 Ion exchange

As ionic semiconductors, ion migration in LHPs is expected to be an important factor for some unusual properties such as current-voltage hysteresis, photoinduced phase transition, and giant dielectric constant.[51] Activation energy (E_a) can be used to evaluate the rate of ion migration that is determined by crystal structure, ionic radius, ion-jumping distance, and charge of ions.[51] As for $MAPbI_3$, a theoretical study suggests that I^- has a much lower E_a (0.58 eV) than MA^+ (0.84 eV) and Pb^{2+} (2.31 eV),[52] which is responsible for the fast halide ion exchange.[53] Although the E_a of Pb^{2+} is much larger, the partial cation exchange of B-site can still be achieved with longer time.[54] Cation exchange usually does not reach completion even when large dopant/Pb ratios are adopted, possibly due to increased lattice strain.[54] Different from the above two approaches, ion exchange always proceeds following the synthesis of LHP NCs or films. For example, colloidal LHP NCs solution are usually first synthesized and dispersed in toluene/hexane solvents. Then, solid dopants or dopant stock solutions with a specific ratio are added into the LHP NCs solution with vigorous stirring. For doped LHP films, the general steps involve the fabrication of LHP films followed by the immersion in the solutions containing dopant ions.[27]

Aiming for fast cation-exchange of the B-site, a simple and effective method, called halide exchange-driven cation exchange (HEDCE), has been proposed and demonstrated

recently (Figure 1a).[55] Partial substitution of Pb sites can be sped up when the rigid $[PbX_6]^{4-}$ octahedra are opened up by halide exchange. This strategy works only if a different halide specie is contained in the dopant precursors. Intriguingly, Mn^{2+}-doped $CsPb(Cl/Br)_3$ NCs can be easily synthesized by adding $MnCl_2$ into $CsPbBr_3$ NCs solution, while cannot be obtained by mixing $MnBr_2$ into $CsPbCl_3$ NCs solution. This is attributed to the difference in ionic radii of halides and dissociation energy of manganese halides.[55, 56] This strategy is also versatile for Sn^{2+}-doped $CsPb(Br/I)_3$ NCs (Figure 1b), in which the thermodynamic balance was broken by the anion exchange, and the cation exchange between Pb^{2+} and Sn^{2+} was therefore promoted.[57] With this HEDCE method, it still takes a long time (~2 days) for ion exchange to complete, since the dopant precursors have a lower solubility in the nonpolar solvent at room temperature.[55] Increasing the solubility of dopant precursors and chance of collision between dopants and host should improve doping efficiency. This has been demonstrated by mixing colloidal solutions of Mn^{2+}-doped $CsPbCl_3$ NCs with $CsPbBr_3$ NCs (Figure 1c), which successfully shortens the reaction time to 1 h.[58] In most situations, LHPs are regarded as hosts to carry out ion exchange. Gao and coworkers demonstrated a reversible cation exchange between $PbCl_2$ and $CsMnCl_3$ NCs at 150 ℃ (Figure 1d),[59] and attribute it to the break of equilibrium of the system once excess capping ligands are introduced. Although E_a of the Pb-site is larger than the other two sites, the highly dynamic nature of capping ligands of LHP NCs greatly promotes the ion exchange between bound and free ions.[59]

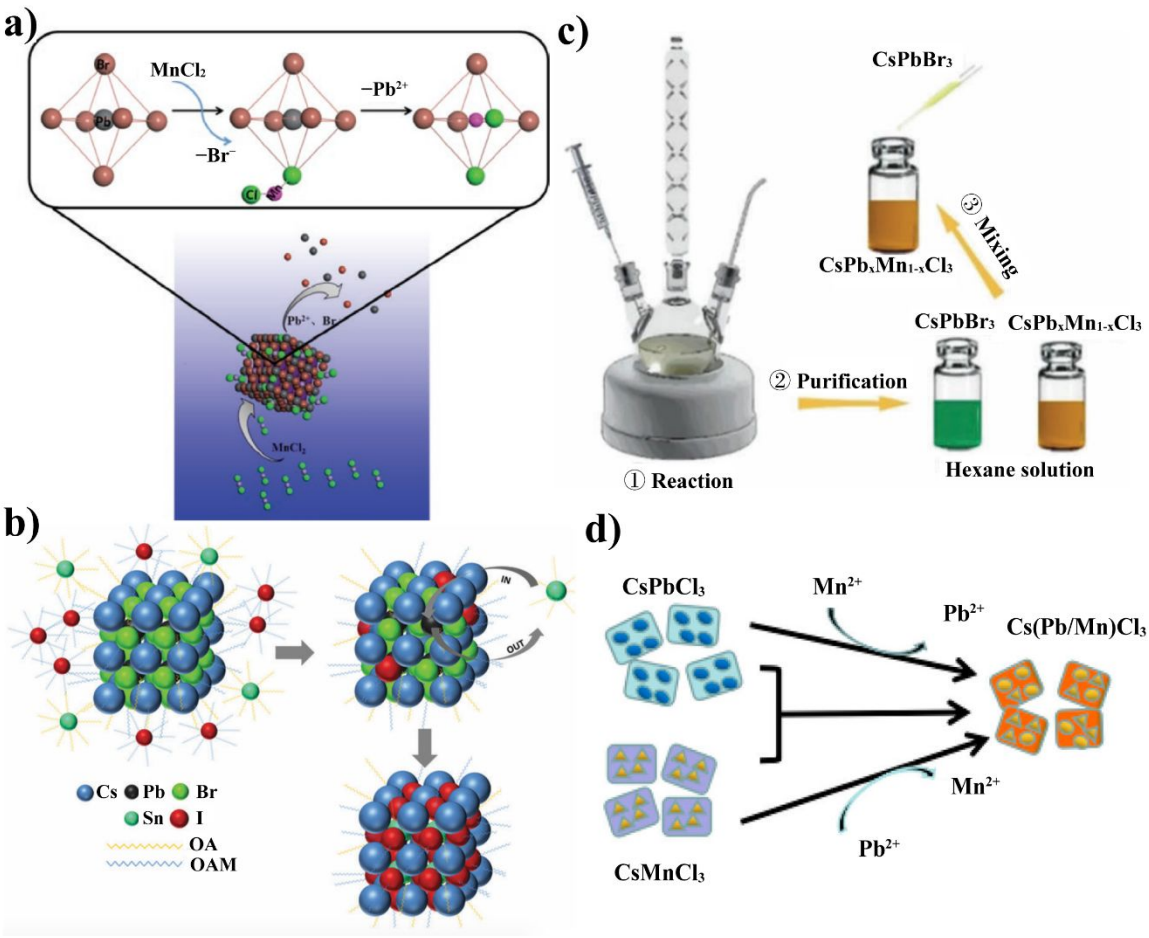

Figure 1. (a) Sketch of HEDCE via adding $MnCl_2$ into $CsPbBr_3$ NCs. (b) Schematic of the ion exchange process in $CsPbBr_3$ NCs upon adding the SnI_2 precursor. (c) Reversible ion exchange between $CsPbCl_3$ and $CsMnCl_3$. (d) Synthesis illustration of $Cs(Pb_xMn_{1-x})(Cl_yBr_{1-y})_3$ NCs obtained by a reversible cation exchange. Adapted with permission from ref 55. Copyright 2017 Wiley. Adapted with permission from ref 57. Copyright 2018 Royal Society of Chemistry. Adapted with permission from ref 58. Copyright 2017 Royal Society of Chemistry. Adapted with permission from ref 59. Copyright 2018 American Chemical Society.

In addition, other strategies such as ultrasonication,[60] melt quenching,[61] spin-coating,[62, 63] solvothermal,[64] antisolvent vapour-assisted crystallization,[65, 66] and inverse temperature crystallization[67] have been also used to prepare NCs, films and single crystals.

3. ELECTRONIC BAND STRUCTURE ENRNEERING AND PHOTOPHYSICS

3.1 Isovalent doping

3.1.1 Sn^{2+} doping. As adjacent element in the same group as Pb, Sn^{2+} is regarded as the first choice to partially substitute Pb^{2+} site because of the high toxicity of Pb.[57, 64, 68, 69] Since $MAPbI_3$ and $MASnI_3$ crystallize in the tetragonal *I4cm* and *P4mm* space groups, respectively, the resulting structure depends strongly on the doping level of Sn^{2+} (Figure 2a).[68] The evolution of two diffraction peaks within the range between 22°−25° confirms the formation of $MASn_{1-x}Pb_xI_3$ solid solutions. Small amount of Sn^{2+} can help to reduce the bandgap and extend the charge carrier lifetime of $MAPbI_3$ LHPs, which is desired for light absorption and solar energy conversion.[69-71] Usually, the bandgap of doped semiconductors is approximately linear with the lattice parameter and compositions according to the empirical Vegard's law.[72] Unexpectedly, the doping of Sn^{2+} has very different impact on the band structure of LHPs. The trend of bandgap change was found to be in the opposite direction once the alloying content of Sn^{2+} is over 50 at.% (Figure 2b),[68, 73] which is in striking contrast with the results reported by others.[71, 74] This is attributed to the competition between spin-orbit coupling (SOC) and lattice distortion.[73] When the concentration of Sn^{2+} ranges from 0 to 50 at.%, the SOC effect dominates and causes

bandgap reduction. Lattice distortion accompanied by phase transition occurs when the molar ration of Pb/Sn is around 1. This anomalous phenomenon is also observed in mixed $MAPb_xSn_{1-x}Br_3$ single crystals, as shown in Figure 2c.[75] Similarly, lattice contraction can result in an increase of orbital overlap, thereby reducing the bandgap of LHPs.[74, 76, 77]

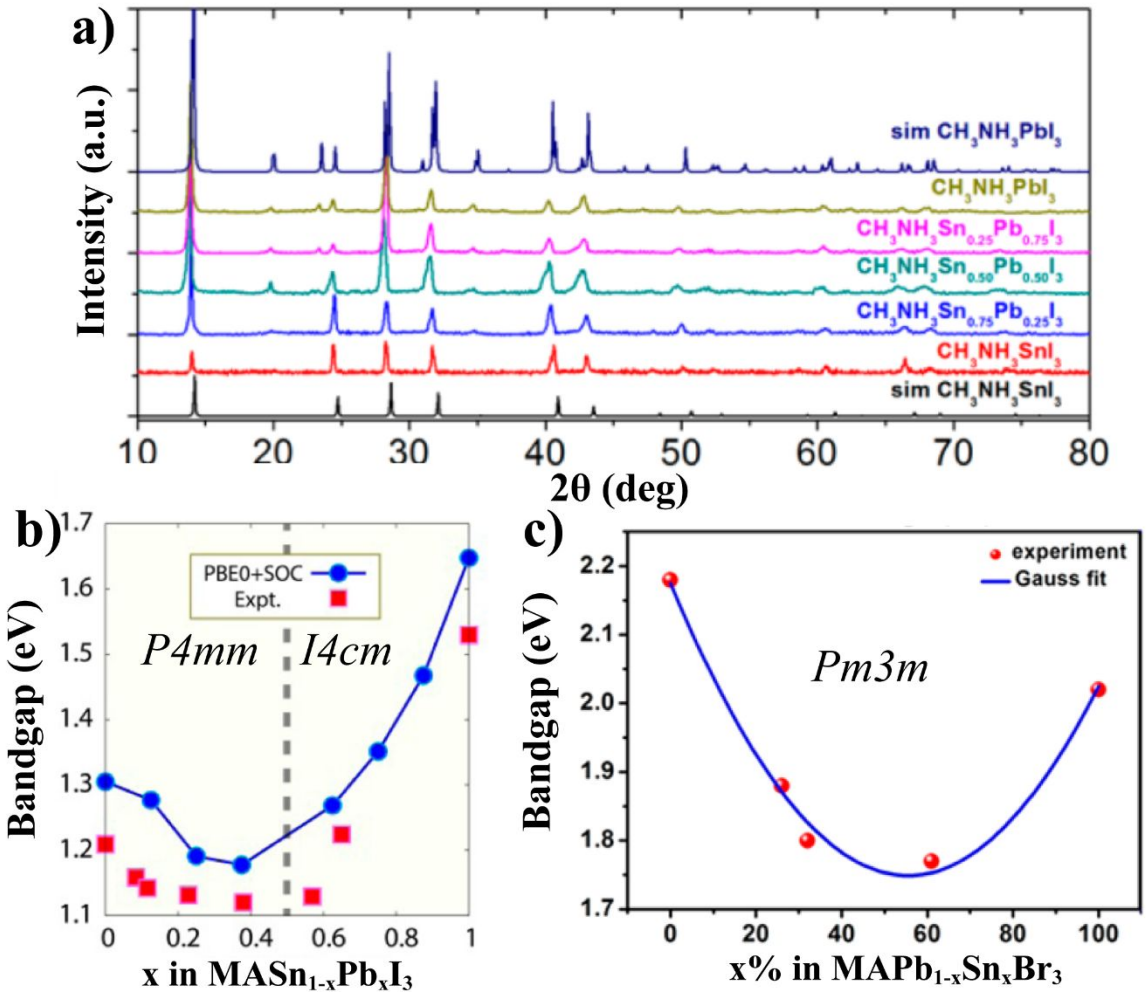

Figure 2. (a) X-ray diffraction pattern of the $CH_3NH_3Sn_{1-x}Pb_xI_3$ solid solutions. (b) Experimental and calculated bandgap evolution of mixed $MASn_{1-x}Pb_xI_3$ as a function of composition x. (c) Experimental bandgap evolution of $MAPb_xSn_{1-x}Br_3$ solid solution as a function of composition x. Adapted with permission from ref 68. Copyright 2014 American Chemical Society. Adapted with permission from

ref 73. Copyright 2015 American Chemical Society. Adapted with permission from ref 75. Copyright 2018 American Chemical Society.

On the contrary, Sn^{2+}-doped $CsPbBr_3$ NCs exhibit a different behavior, with bandgap increasing with partial Sn^{2+}-substitution.[78, 79] For example, the PL of $CsPb_{1-x}Sn_xBr_3$ NCs can be tuned towards shorter wavelength by increasing the Sn^{2+} content (Figure 3a).[79] Similarly, divalent ions, including Cd^{2+} and Zn^{2+}, were successfully doped into $CsPbBr_3$ NCs through cation exchange.[54] With these smaller cations, the PL blue-shifts linearly with the lattice contraction (Figure 3b),[54] attributed to the valence band maximum (VBM) shifting less than the conduction band minimum (CBM) with lattice contraction.[54] Based on first-principles calculations shown in Figure 3c, the CB of LHPs is mainly derived from the s orbitals of the metal with less contribution from the p orbitals of the halogen, which indicates that CBM would shift less with respect to VBM upon lattice contraction and distortion.[77] Given the great effect of the radii of A, B and X-sites on lattice distortion/contraction, different species of A and X-sites may lead to anomalous phenomenon upon doping of B-site. For instance, Sn^{2+}-doped $CsPbBr_3$ and $MAPbBr_3$ show totally different trends in terms of the bandgap of host.[74, 79] Detailed theoretical and experimental studies are necessary in the future to better understand the difference.

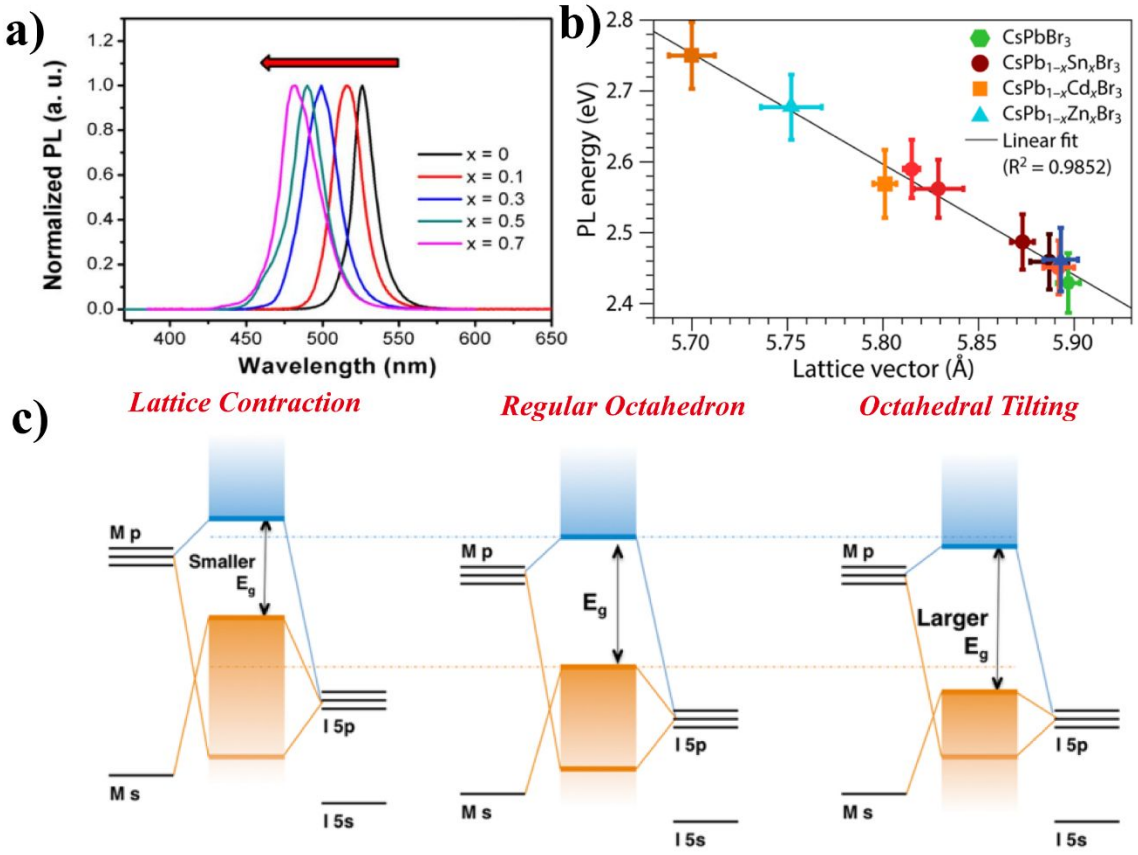

Figure 3. (a) PL spectrum of $CsPb_{1-x}Sn_xBr_3$ NCs as a function of Sn content (x = 0-0.7). (b) PL energy as a function of the lattice vector in doped $CsPb_{1-x}M_xBr_3$ (M= Sn, Cd, and Zn) NCs. (c) Schematic energy level diagram of the evolution of VB and CB affected by contraction and distortion. Adapted with permission from ref 79. Copyright 2016 Elsevier. Adapted with permission from ref 54. Copyright 2017 American Chemical Society. Adapted with permission from ref 77. Copyright 2017 American Chemical Society.

3.1.2 Alkaline-earth cations doping. The easy oxidation of Sn^{2+} to Sn^{4+} upon exposure to atmosphere presents a major challenging for use as a dopant.[28, 45] To search for other more stable metal halide perovskites with suitable bandgap, the substitution of Pb^{2+} with all

isovalent metal ions have been explored through computational screening.[80] For instance, partial substitution of Pb^{2+} by alkaline-earth cation Mg^{2+} was suggested as a possibility according to simulation results. Similar simulations were also conducted on other alkaline-earth cations including Ca^{2+}, Sr^{2+} and Ba^{2+} based on Goldschmidt's rules.[81, 82] Although the complete replacement of Pb^{2+} by these alkaline-earth cations results in wide bandgap (2.9~3.3 eV) and poor absorption,[81, 82] low level doping with alkaline-earth cations is an effective strategy to tailor the structural, morphological and optoelectronic properties of LHPs films. For example, the doping of Ca^{2+} results in a slight decrease of the bandgap and the formation of cubic $MAPbI_3$.[78, 83]

Similarly, doping with Sr^{2+} causes a reduction of $MAPbI_3$ bandgap.[78, 84] Compared to the small radius of Ca^{2+} (1.00 Å), Sr^{2+} (1.18 Å) is almost identical to that of Pb^{2+} (1.19 Å), which eliminates the impact on structural distortion and contraction. In addition, the lifetime of charge carriers in $MAPbI_3$ is significantly improved after the introduction of Sr^{2+} (Figure 4a and b) and the charge separation efficiency is subsequently enhanced.[85] Likewise, the recombination lifetime is improved from 11.1 to 17.1 ns upon doping with 2% Sr^{2+},[63] which may originate from effective passivation by the Sr-enriched surface.[63, 85] Doping often induces the formation of defects, which can trap photogenerated electrons and holes and reduce the lifetime of emission. For instance, the average PL lifetime dramatically decreases from 200 to 60 ns after the introduction of Sr^{2+} (Figure 4c and d).[84] Despite the small drop of solar power conversion efficiency, the incorporation of Sr^{2+}

improves the thermal stability and output voltage, attributed to the suppression of Pb^0 and up-shift of CBM, respectively.[84]

Ba^{2+}, as another alkaline metal ion, has also been investigated to tune the optical and electronic properties of LHPs films. The addition of small amount of Ba^{2+} is beneficial to the growth of smooth films and larger crystallites, thereby enhancing the carrier transport.[62] Compared to Pb^{2+}, Ba^{2+} with smaller electronegativity binds I^- more strongly, which may affect the band structure of the host. The incorporation of Ba^{2+} into the lattice lifts the CBM and enlarge the bandgap (Figure 4e), as indicated by the absorption spectrum (Figure 4f).[86] This is attributed to the distortion and weak Pb-I bond because of the larger radius (1.35 Å) and smaller electronegativity of Ba^{2+}.[86]

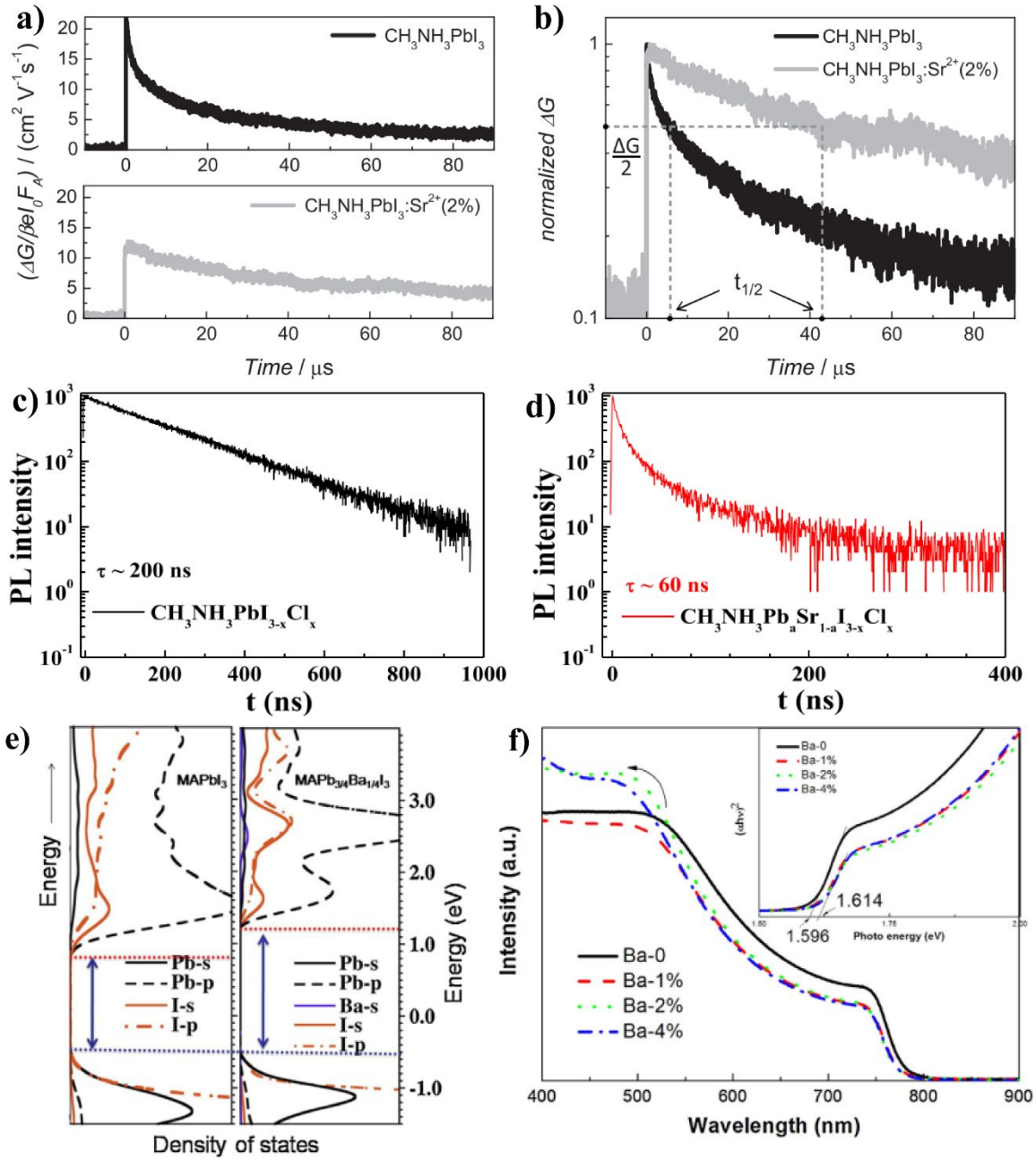

Figure 4. (a) Comparison of the normalized time-resolved microwave conductivity (TRMC) traces for the same samples. (b) time-resolved PL decay profiles of $CsPb_{1-x}Sr_xI_2Br$ films. Time-resolved PL spectra of undoped $MAPbI_{3-x}Cl_x$ (c) and doped $MASr_aPb_{1-a}I_{3-x}Cl_x$ (d) perovskite films. (e) Density of states (DOS) of $MAPbI_3$ and $MAPb_{3/4}Ba_{1/4}I_3$. (f) The UV-visible absorption spectra of Ba^{2+} doped and undoped perovskite films, the insert is $(\alpha h\upsilon)^2$ versus light excitation energy hυ. Adapted with permission

from ref 85. Copyright 2016 Wiley. Adapted with permission from ref 84. Copyright 2017 Elsevier. Adapted with permission from ref 86. Copyright 2017 Elsevier.

3.1.3 Mn^{2+} doping. Mn^{2+}, as a transition metal cation, has been intensively studied in II-VI semiconductor NCs due to its capability to endow hosts with paramagnetism and new emission band, as a result of strong exchange interaction between charge carriers of the host and d-electrons of the Mn^{2+} dopants.[35, 36] Because the activation of spin relaxation of Mn^{2+} is induced by the energy transfer from the host exciton to Mn^{2+}, the emission of Mn^{2+} strongly depends on the bandedge position and bandgap of host.[87] LHPs with tunable bandgap resulting from varying the species and ratios of halogen are ideal as host for Mn^{2+} doping.

Two studies of Mn^{2+}-doped $CsPbCl_3$ NCs were reported simultaneously in 2016,[29, 30] which triggered intensive investigations on Mn^{2+} doping.[43, 48, 58, 59, 88-95] The successful incorporation of Mn^{2+} can be indicated by the shift of towards larger scattering angle in the XRD pattern owing to the smaller radius of Mn^{2+} (0.97 Å) compared to to Pb^{2+} (1.19 Å),[29] and electron paramagnetic resonance (EPR) signal because of the high spin state of Mn^{2+} in the octahedron.[30] Strong dopant emission centered at ~600 nm is observed after introducing Mn^{2+} into the lattice of $CsPbCl_3$ NCs (Figure 5a and b). Interestingly, Mn^{2+} cannot be directly incorporated into $CsPbBr_3$ and $CsPbI_3$ via a hot-injection method, but its doping can be achieved through anion-exchange. This is possibly related to the disparity of dissociation energy between Pb-X and Mn-X.[29] Replacement of Pb^{2+} by Mn^{2+} is more

likely if the dissociation energy of Mn-X bond is comparable to that of Pb-X. Besides Cl-based LHPs, Mn^{2+} emission (~2.10 eV) is expected in $CsPbBr_3$ host with a bandgap of 2.50 eV (Figure 5c).[96] However, the PL of Mn^{2+} is rarely observed in $CsPbBr_3$ or $CsPbI_3$ host because of their inappropriate bandedge positions and narrow bandgap. Mn^{2+}-doped $CsPbBr_3$ NCs can be obtained via the formation of an intermediate structure through hot-injection method.[97] The prepared Mn^{2+}-doped $CsPbBr_3$ NCs exhibit strong dopant emission when the host bandgap is enlarged, as shown in Figure 5d.

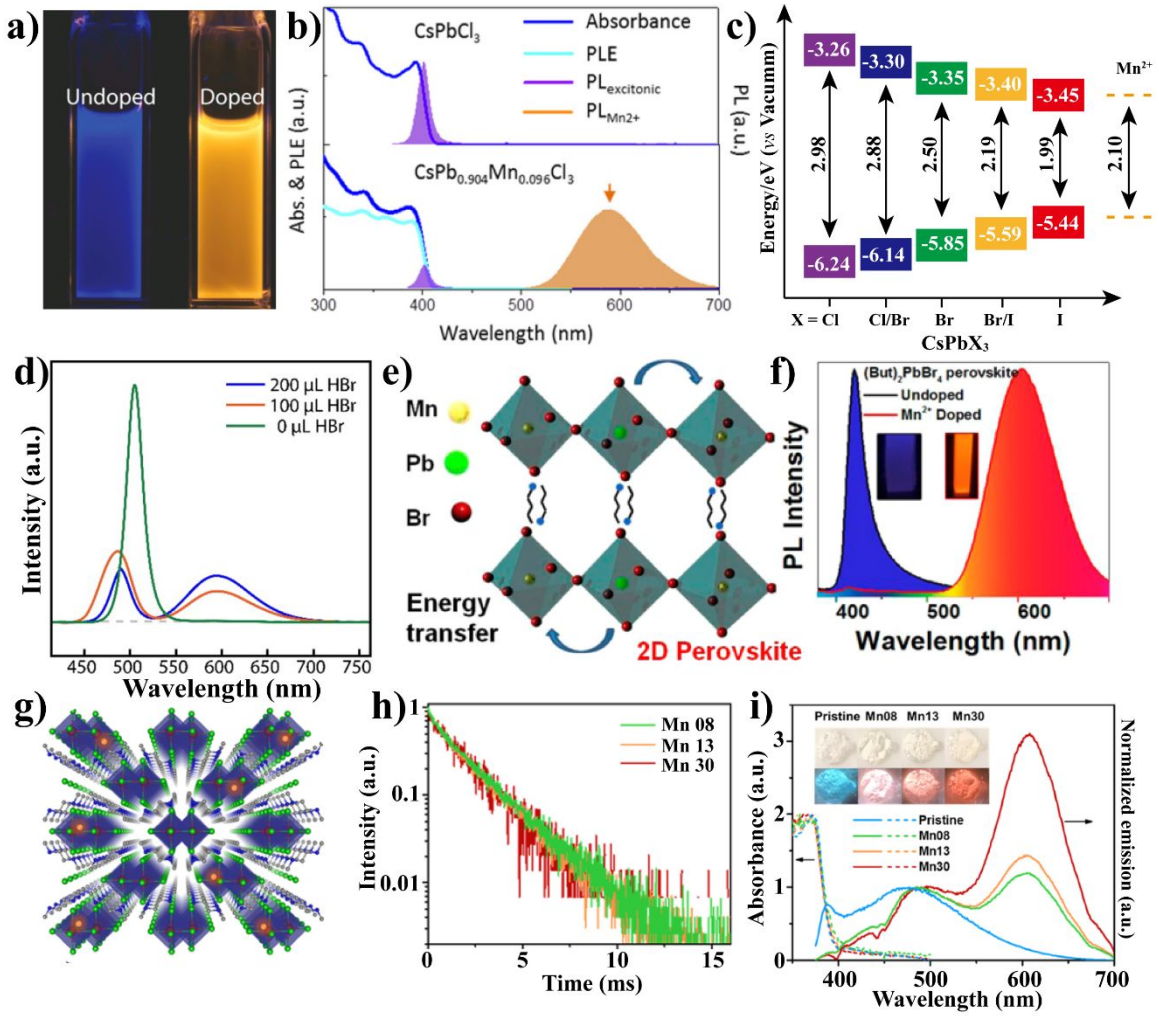

Figure 5. (a) Photographs of the undoped and Mn^{2+}-doped $CsPbCl_3$ NCs under UV excitation. (b) The optical properties of undoped (top) and Mn^{2+}-doped (bottom) $CsPbCl_3$ NCs. (c) Band positions of $CsPbX_3$ and Mn^{2+} d-states. (d) PL spectra of Mn^{2+}-doped $CsPbBr_3$ nanocubes synthesized with varying amount of HBr. (e) Schematic representation of the bulk phase of n = 1 of $(L)_2(L')_{n-1}Pb_nX_{3n+1}$ 2D perovskite. (f) PL spectra of undoped and Mn^{2+}-doped 2D perovskite. (g) Schematic representation of 1D $C_4N_2H_{14}PbBr_4$ perovskite. (h) PL decay profiles of the pristine and Mn^{2+}-doped 1D lead bromide perovskites monitored at 650 nm. (i) Absorption (dashed line) and emission (solid line) spectra of the pristine and Mn^{2+}-doped 1D, the inset shows the images of the pristine and Mn^{2+}-doped 1D $C_4N_2H_{14}PbBr_4$ perovskite under ambient light (top) and UV light (365 nm, bottom). Adapted with permission from ref 30. Copyright 2016 American Chemical Society. Adapted with permission from ref 29. Copyright 2016 American Chemical Society. Adapted with permission from ref 96. Copyright 2016 American Chemical Society. Adapted with permission from ref 97. Copyright 2016 American Chemical Society. Adapted with permission from ref 98. Copyright 2017 American Chemical Society. Adapted with permission from ref 49. Copyright 2017 American Chemical Society.

Similar strategies were also used on low dimensional Br-based LHPs.[49, 98] Such strong quantum confinement in low dimensional systems can further enhance the dopant-host exchange interaction and boost energy transfer. Mn^{2+} doping in single-layered $(C_4H_9NH_3)_2PbBr_4$ has been achieved via simple grounding and post-annealing (Figure 5e and f),[98] Mn^{2+} emission shows a high QY of 37% and lifetime of 0.74 ms in $(C_4H_9NH_3)_2PbBr_4$. This method works very well for a variety of single-layered LHPs with

different spacing ligands but does not work for 3D LHPs. Since single-layered LHPs have more exposed Pb-sites for anion exchange compared to 3D systems, more efficient or faster exchange in 2D hosts is anticipated. Similarly, 1D $C_4N_2H_{14}PbBr_4$ with a broad emission band was also utilized as host for Mn^{2+} doping (Figure 5g).[49] $C_4N_2H_{14}PbBr_4$ presents a broadband emission at room temperature due to the self-trapped exciton, which is usually observed in low dimensional materials. Mn^{2+} emission exhibits extremely long lifetime of 2 ms, further confirming successful doping (Figure 5h). By combining the broad blue emission from self-trapped states and strong orange yellow emission from Mn^{2+} d-d transition, white light emission with color rendering index (CRI) of 87 is successfully realized (Figure 5i).

In general, introduction of dopants into host lattices tends to result in the formation of defects that decrease intrinsic host emission. Emission from dopants such as Mn^{2+} usually competes with bandedge emission, which is expected to decrease after Mn^{2+} doping. Intriguingly, low level doping of Mn^{2+} in $CsPbCl_3$/$MAPbCl_3$ NCs has been found to not only generate new dopant emission, but also boost excitonic emission (Figure 6a and b), which contradicts the traditional exciton energy transfer notion.[30, 43, 50, 99-101] Parobel *et al*. proposed that doping of Mn^{2+} may remove some of the preexisting defects and alter the competing kinetics between radiative and nonradiative relaxation.[30] In comparison with Br- and I-based LHP NCs, the excitonic emission of $CsPbCl_3$ NCs is usually much lower (QY < 5%), indicating that Mn^{2+} emission in doped $CsPbCl_3$ with overall QY of ~20-60% is mainly competing with nonradiative recombination. Wei and coworkers found that the

build-up time of Mn^{2+} emission was much longer (206 ± 16 ns) than that of bandedge emission (< 10 ns), and close to the typical trap-state decay time (Figure 6c),[102] suggesting that the energy transferred to Mn^{2+} is mainly from the nonradiative trap states rather than bandedge states (Figure 6d), consistent with the observation of increased bandedge emission with low level Mn^{2+} doping.

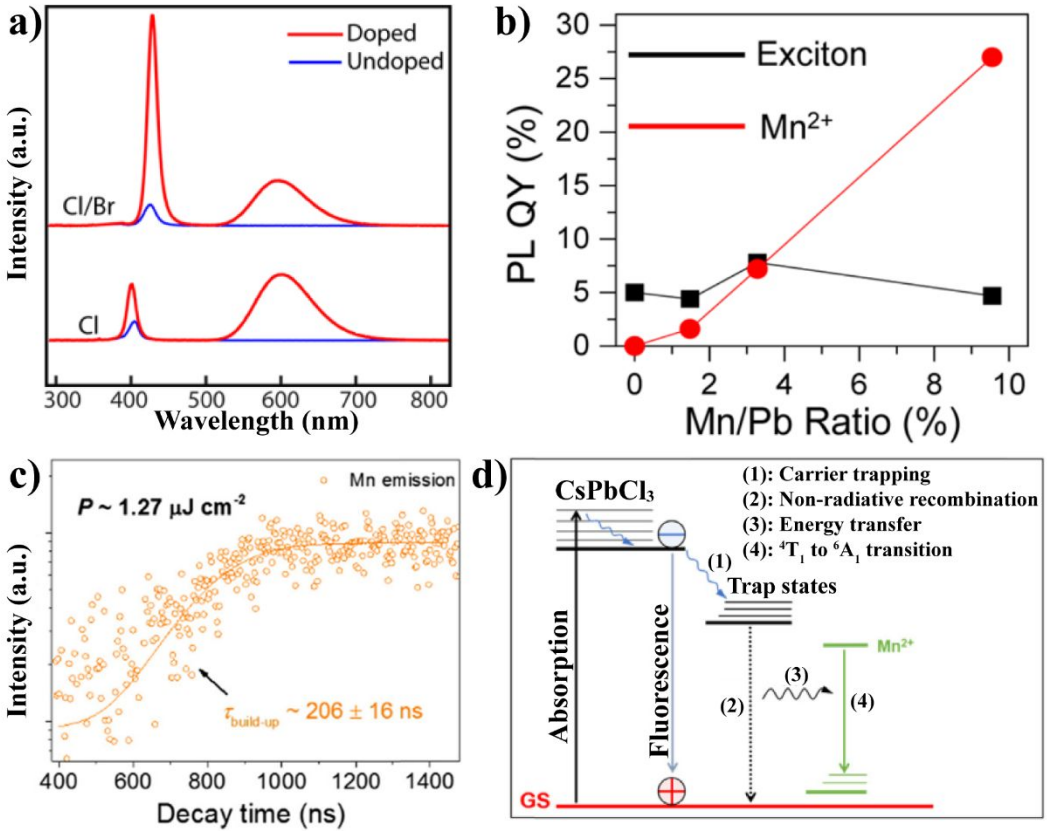

Figure 6. (a) PL of Mn^{2+}-doped and undoped $CsPbCl_3$ and $CsPb(Cl/Br)_3$ NCs. (b) Absolute PL QY of the bandedge emission and Mn dopant emission. (c) TRPL curves monitored at the Mn emission (orange circles) with fitted curves (solid lines) under 1.27 μJ cm^{-2} excitations. (d) Schematic energy levels and electronic transitions in Mn^{2+}-doped NCs. Adapted with permission from ref 30. Copyright 2016

American Chemical Society. Adapted with permission from ref 29. Copyright 2016 American Chemical Society. Adapted with permission from ref 102. Copyright 2018 Elsevier.

To achieve high QY of Mn^{2+} emission requires optimization of its doping level. However, usually only a small fraction of Mn^{2+} can be introduced into LHP NCs. For instance, Mn^{2+}:Pb^{2+} in a 1:1 nominal molar ratio only results in the replacement of 6.7% Pb^{2+} sites.[14] By elevating the reaction temperature and molar feed ration of Mn^{2+}:Pb^{2+}, the Mn substitution can be increased up to 46% with an optimal overall QY of 54% for $CsPbCl_3$ NCs (Figure 7a) via a hot injection approach.[42] Similarly, Yuan and coworkers obtained Mn^{2+}-doped $CsPbCl_3$ with a maximum atomic ratio of 14.6% and QY of ~60%.[41] Interestingly, mixed $CsPbX_3$ with Mn^{2+} doping ratio of 37.7% is easily achieved at room temperature via the LARP method (Figure 7b).[103] Similarly, Arunkumar and coworkers successfully elevated the Mn^{2+} doping level to 90% in mixed hybrid organic-inorganic LHP NCs (Figure 7c).[104] However, the content of Mn^{2+} may have contributions from ions adsorbed on the surface of NCs in this case since no purification was done for the prepared samples.

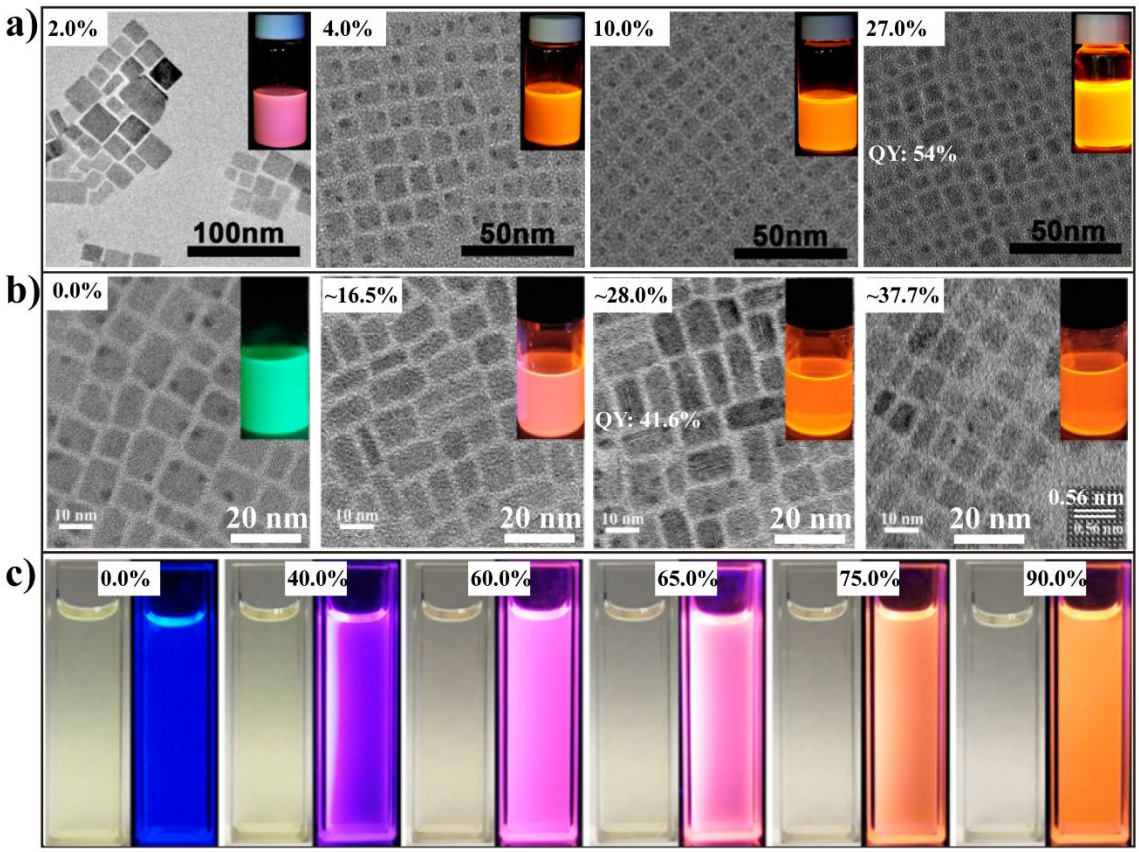

Figure 7. (a) TEM images of the $CsPb_xMn_{1-x}Cl_3$ QDs that are prepared with different Pb-to-Mn molar feed ratios. (b) TEM images of as-prepared NCs with Mn-to-Pb molar feed ratios. (c) Images of QDs in the visible (left side) and 365 nm UV light (right side). The actual doping efficiency is labeled on top of pictures. Insets: Corresponding PL images excited by 365 nm UV light. Adapted with permission from ref 52. Copyright 2017 American Chemical Society. Adapted with permission from ref 103. Copyright 2017 American Chemical Society. Adapted with permission from ref 104. Copyright 2017 American Chemical Society.

Due to competition between bandedge and dopant emission, temperature may show different impacts on them, which could help to understand the energy transfer process. For

example, a study shows that upon lowering the temperature, the bandedge emission at 390 nm blue shifts slightly with greatly enhanced intensity, while dopant emission shows a red shift with reduced intensity (Figure 8a).[42] Such evolution is consistent with thermally active exciton-to-dopant energy transfer (Figure 8b). Femtosecond transient absorption (TA) further confirms the competing relationship between carrier trapping and exciton-to-dopant energy transfer.[43] With a low doping level (2%), both the lifetime and amplitude of the slow component (representing the lifetime of nonradiative recombination via bandedge) increase (Figure 8c), indicating partial removal of pre-existing structure defects, consistent with the increased intensity of bandedge emission. With respect to carrier trapping, the much longer lifetime of exciton-to-dopant energy transfer suggests that the introduction of Mn^{2+} has very limited impact on carrier trapping. By increasing the doping level (12%), the bleach recovery becomes faster, resulting from prominent energy transfer from LHPs host to Mn^{2+} dopants. The time scale of this energy transfer is estimated to be ~50-100 ps, which highly depends on the doping content. In addition, high dopant concentrations induce exchange interaction of Mn^{2+}-Mn^{2+} pairs that results in fast decay dynamics as well as a red-shift of dopant emission (Figure 8d). In this case, only the carrier trapping and nonradiative recombination processes on ps time scale are observed due to the short time window. To more completely determine the exciton dynamics, longer monitoring time window (ns) is necessary. Rossi and coworkers compared the exciton dynamics of Mn^{2+}-doped $CsPbCl_3$ and Mn^{2+}-doped CdS/ZnS core/shell QDs on ns time scale (Figure 8e and f).[99] In this case, the fastest component with a few ps lifetime is attributed to the carrier

trapping by defects, while the ns recovery component is attributed to radiative and slower nonradiative recombination. Different from the pristine sample, an additional recovery component with 380 ps lifetime is observed in Mn^{2+}-doped $CsPbCl_3$, which is due to exciton-to-dopant energy transfer. Compared to Mn^{2+}-doped $CsPbCl_3$, the coupling interaction between exciton and Mn^{2+} dopants in CdS/ZnS core/shell QDs are much stronger with shorter energy transfer time of 70-190 ps, consistent with other studies.[43]

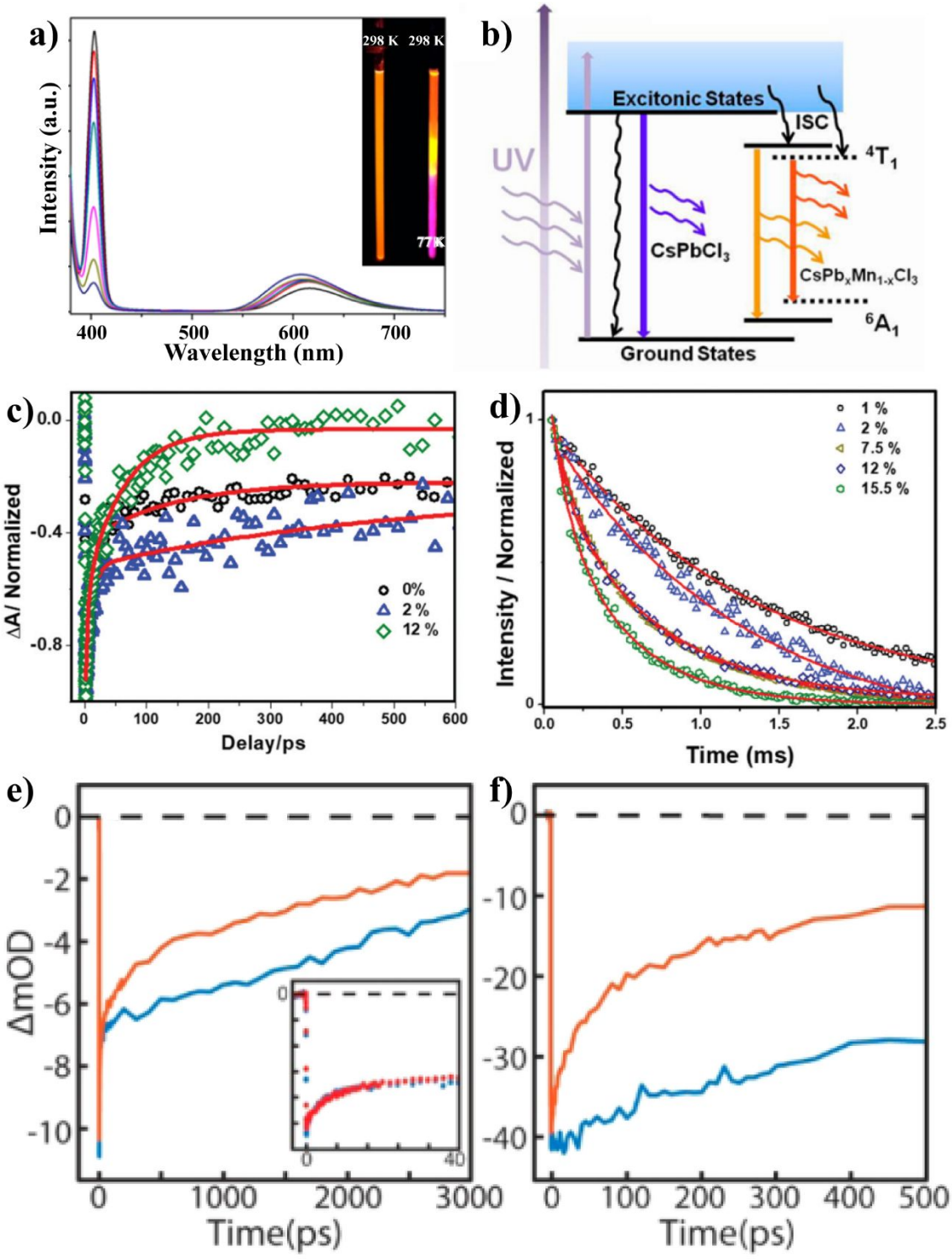

Figure 8. (a) Temperature-dependent emission spectra of the $CsPb_{0.73}Mn_{0.27}Cl_3$ QDs. (b) Energy levels and fluorescent mechanism of $CsPb_xMn_{1-x}Cl_3$ QDs, where ISC represents intersystem crossing. (c) Comparison of bleach recovery kinetics of 0, 2% and 12% Mn^{2+}-doped $CsPbCl_3$ NCs, monitored at their

excitonic bleach maxima. (d) Mn PL (λ_{exc} = 330 nm) decay behavior of the samples monitored at their respective emission maxima. (e) Transient absorption data of undoped (blue) and Mn^{2+}-doped (red) $CsPbCl_3$ NCs with 395 nm pump and 400 nm probe. (f) Transient absorption data of undoped (blue) and Mn^{2+}-doped (red) CdS/ZnS core/shell QDs. Adapted with permission from ref 42. Copyright 2017 American Chemical Society. Adapted with permission from ref 43. Copyright 2017 Royal Society of Chemistry. Adapted with permission from ref 99. Copyright 2017 American Chemical Society.

Motivated by the higher formation energy of $CsMnX_3$, the strategy for enhancing the air and thermal stability of LHPs through Mn^{2+}-doping was proposed.[100] First-principles calculations were conducted to determine the formation energy (ΔE_{form}, defined as the change in energy when a NC is formed from its isolated atoms) and some bond lengths of $CsMnBr_3$, $CsPbBr_3$, and $CsPbBr_3$:Mn NCs. The absolute value of ΔE_{form} per Pb^{2+} (or Mn^{2+}) ion was found to rise slightly with increased Mn^{2+} content, reaching a maximum at ~2.08 mol %, and then to decrease rapidly with further increasing the doping content of Mn^{2+} in $CsPbBr_3$ NCs. The rise of ΔE for doped $CsPbBr_3$ NCs enhances its thermal stability. To evaluate the thermal stability of $CsPbX_3$:Mn NCs induced by Mn^{2+} doping, the temperature dependent PL emission spectra for pure $CsPbX_3$ and $CsPbX_3$:Mn NCs in the range from 77 K to 473 K were compared. As shown in Figure 9a, enhanced excitonic luminescence was clearly observed in Mn^{2+}-doped $CsPbBr_3$ QDs after three heating/cooling cycles at 100, 150, and 200 °C, much better than that of pure $CsPbBr_3$. This approach also works well for Cl- and I- based LHPs.[18, 100] The excitonic emission was substantially enhanced

with high level of Mn^{2+} doping (Figure 9b). Such enhanced emission stems from excess Mn^{2+} dopants gradually excluded from the lattices of $CsPbX_3$ NCs when heated at high temperature.

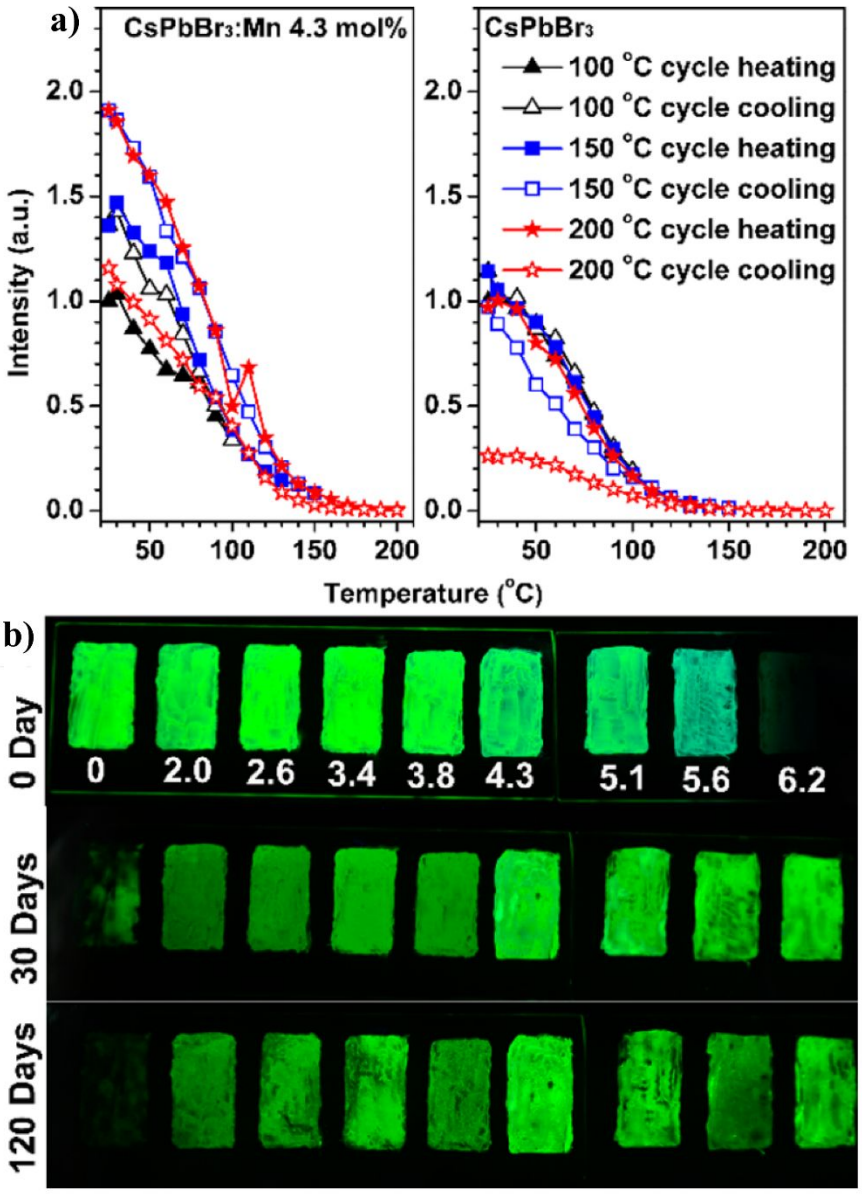

Figure 9. (a) Temperature-dependent PL intensities for excitonic luminescence of $CsPbBr_3:Mn^{2+}$ (4.3 mol %) and pure $CsPbBr_3$ NCs via three heating/cooling cycles at 100, 150, and 200 °C, respectively. (b) PL emission photographs for $CsPbBr_3:Mn^{2+}$ NCs coated on the surface of a glass slide with different

Mn^{2+} contents from 0 to 6.2 mol %. Adapted with permission from ref 100. Copyright 2017 American Chemical Society.

3.1.4 Doping with other transition metals. Besides Mn^{2+}, other transition metal ions have also been used to dope LHPs. For example, Cd^{2+} and Zn^{2+} were doped into $CsPbBr_3$ NCs to tune the PL emission in the range of 452~512 nm.[54] Since the ionic radius of both Cd^{2+} (0.95 Å) and Zn^{2+} (0.74 Å) is smaller than that of Pb^{2+}, doping with these two ions induces contraction of lattice, causing the blue-shift of the host PL. Dopant ions with the same coordination mode and number as the host ion are favored for doping efficiency and stability of lattice structure. Divalent Ni^{2+} (radius ~0.69 Å) prefers octahedral coordination with halide ions and is a potentially good dopant for LHPs. A general strategy for the synthesis of violet-emitting LHP NCs with near-unity PL QY through Ni^{2+} doping has been reported (Figure 10a).[46] Although no dopant emission was observed at room or cryogenic temperature, the PL QYs of bandedge emission was greatly improved from 2.4% for undoped $CsPbCl_3$ NCs to 96.5% for 11.9% Ni^{2+}-doped $CsPbCl_3$. Extended X-ray absorption fine structure (EXAFS) spectra further demonstrate that the order of local coordination environment of Pb^{2+} is improved after introducing $NiCl_2$ during the synthesis, suggesting the removal of structural defects and improved short-range order of the lattice. This is consistent with density functional theory (DFT) simulation results that the introduction of Ni^{2+} can notably increase the formation energy of Cl, Cs and Pb vacancies. Both the excitonic absorption and PL peak shift to blue slightly caused by lattice

contraction. As shown in Figure 10b, the PL lifetime becomes longer with Ni^{2+} doping, indicating suppression of non-radiative recombination upon doping. Importantly, this concept is not only applicable to Cl-based LHPs, but also to mixed LHPs (Figure 10c). Recently, the doping of Co^{2+} was found to induce a transition of $MAPbI_3$ from tetragonal phase to cubic phase due to the small radius of Co^{2+} (0.74 Å at high spin state).[105] With the increase of Co^{2+} concentration, both the absorption and emission shift to red slightly, probably caused by the decreased d-spacing. In addition, the larger grain size, enhanced electrical conductivities and charge carrier mobility of Co-doped $MAPbI_3$ improve PV performance.

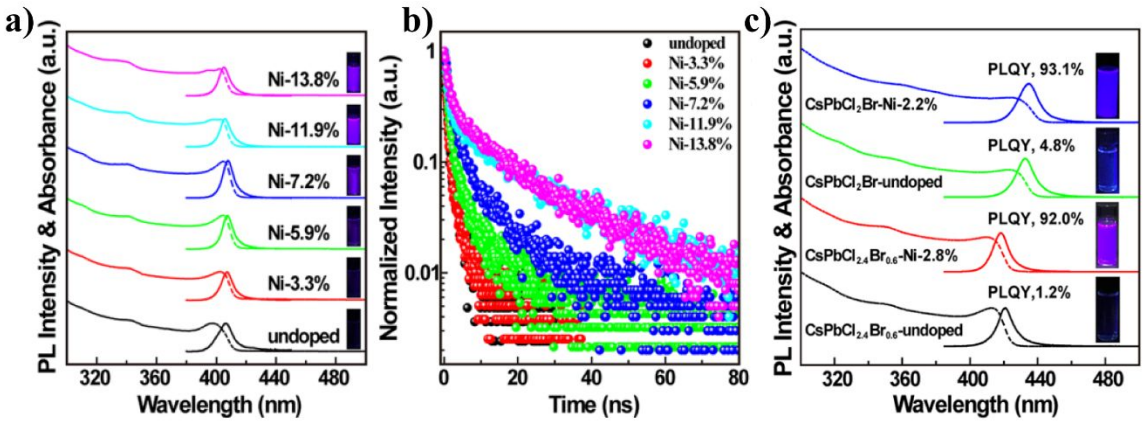

Figure 10. (a) Absorption and PL spectra of undoped and doped $CsPbCl_3$ NCs. (b) PL decay traces of undoped and doped $CsPbCl_3$ NCs. (c) Absorption and PL spectra of undoped and doped $CsPb(Cl,Br)_3$ NCs. Inset: photographs of NCs solution under UV (365 nm) illumination. Adapted with permission from ref 46. Copyright 2018 American Chemical Society.

3.2 Heterovalent doping

3.2.1 Bi^{3+} doping. Heterovalent doping can effectively switch the sign of majority charge carriers in semiconductor materials and enhance electrical conductivity and mobility.[34] Bi^{3+} is isoelectronic with Pb^{2+} and its radius (1.03 Å) is also close to that of Pb^{2+}, indicating a possible good fit of Bi^{3+} into the perovskite. Abdelhady and coworkers showed an *in situ* chemical route of achieving trivalent cations (Bi^{3+}, Au^{3+} or In^{3+}) doped $MAPbBr_3$ single crystals.[106] By increasing the Bi^{3+} concentration in feed solution, the color of $MAPbBr_3$ single crystal turns black gradually (Figure 11a). More interestingly, the absorption onset shifts from 570 nm for the undoped crystal to 680 nm for the 10% Bi^{3+}-doped LHPs (Figure 11b). It was suggested that the introduction of Bi^{3+} alters the density of states and the higher electronegativity of Bi^{3+} leads to more covalent bonding with bromide, thereby narrowing the bandgap. This behavior is also observed in other Bi^{3+}-doped LHPs.[65, 67] As an intrinsic p-type semiconductor,[107] the sign of the majority carrier of $MAPbBr_3$ has been successfully converted to n-type upon Bi^{3+} doping. In addition, the conductivity is enhanced as much as 4 orders of magnitude and free carrier concentration increases from ~10^9 cm^{-3} (undoped crystals) to ~10^{11}-10^{12} cm^{-3} (Figure 11c).

Note that the shape of the absorption curves are not as sharp as that of the undoped crystals (Figure 11b), which is likely due to the contribution from absorption of bandgap states or the thick LHPs samples used.[66] To determine the real cause, a series of careful measurements including absorption spectrum (Figure 11d), spectroscopic ellipsometry (Figure 11e), microstrain test and solid-state nuclear magnetic resonance (NMR) were

conducted by Nayak and colleagues.[108] The results indicate that the apparent color change of Bi^{3+}-doped LHPs is due to the increased number of defect states within the bandgap, which also facilitate the nonradiative recombination of excitons and lower the PL intensity and lifetime.[108]

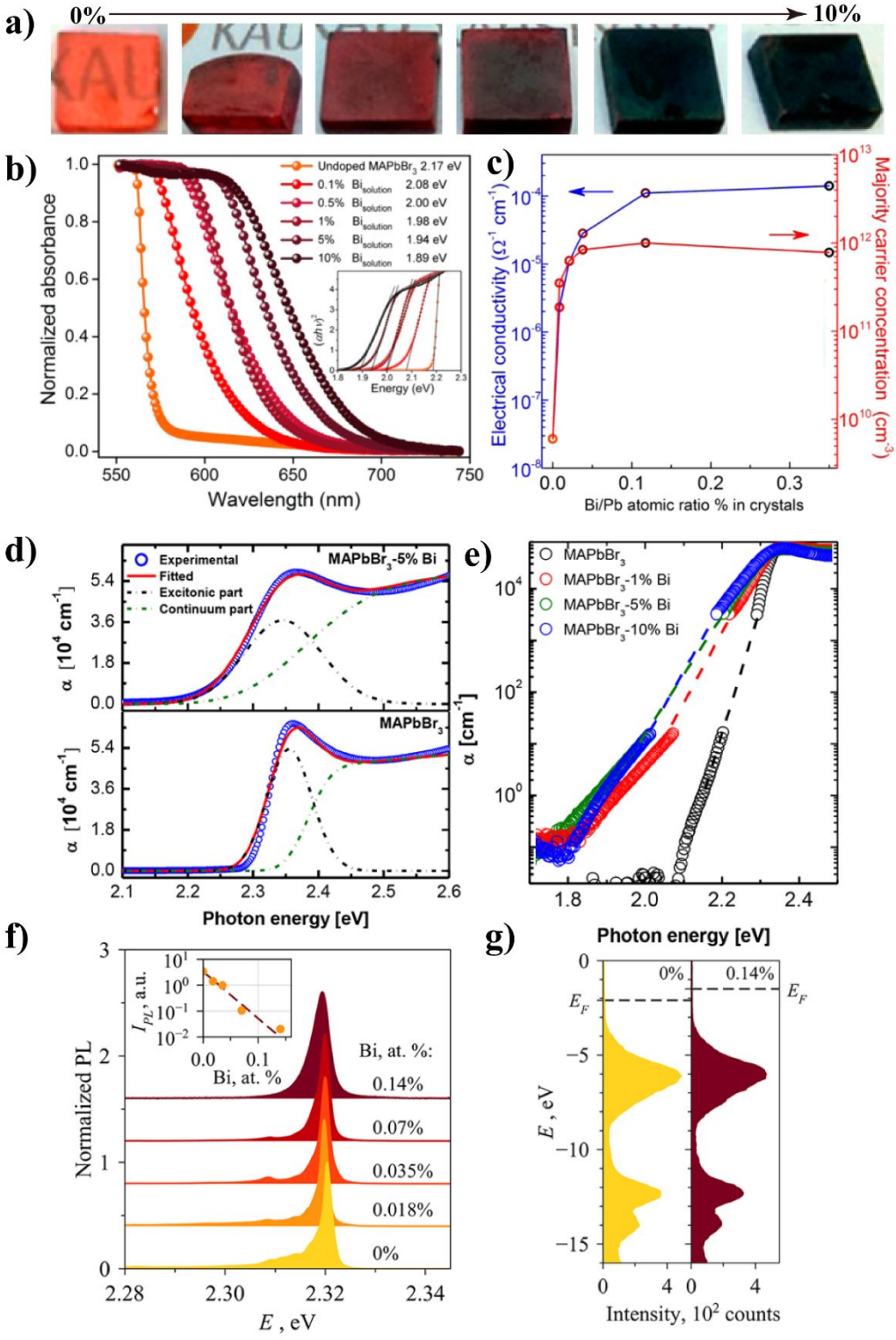

Figure 11. (a) Photographs showing $MAPbBr_3$ crystals having various Bi incorporation levels. (b) Steady-state absorption spectra of $MAPbBr_3$ crystals with various Bi%. Inset: corresponding Tauc plots.

(c) Conductivity and majority charge concentration of the different crystals as a function of Bi/Pb atomic ratio % in the crystals. (d) Absorption spectra in the bandedge region for a $MAPbBr_3$ single crystal (bottom) and a $MAPbBr_3$ single crystal with 5% Bi^{3+} doping (top). (e) Combined absorption spectra from ellipsometry data (top part) and the UV−vis transmission data (bottom part). The dashed lines are the guides to the eye only. (f) Normalized low-temperature (3.6 K) PL spectra of $CsPbBr_3$ single crystals doped with Bi^{3+}. The dependence of the exciton peak intensity on Bi^{3+} concentration is plotted in the inset. (g) Ultraviolet Photoelectron spectroscopy (UPS) and positions of the Fermi level (E_F) for pristine and Bi^{3+}-doped $CsPbBr_3$ single crystals. Adapted with permission from ref 106. Copyright 2016 American Chemical Society. Adapted with permission from ref 108. Copyright 2018 American Chemical Society. Adapted with permission from ref 109. Copyright 2018 American Chemical Society.

However, a recent study found no evidence of bandgap narrowing for Bi^{3+}-doped $CsPbBr_3$ LHPs, in which the excitonic luminescence peak remains unaffected at the temperature of 3.6 K (Figure 11f).[109] No changes of the position and state distribution of the VB and Fermi level are observed after Bi^{3+} doping (Figure 11g). This clearly contradicts other studies, and further study is necessary to clarify the different observations.

The substitution of Pb^{2+} by Bi^{3+} was considered to possibly result in the increase of defect density of LHPs and distortion of crystal lattice, which may lead to ultrabroad emission once the distorted lattices couple with photogenerated excitons.[49] As shown in Figure 12a, the insertion of Bi^{3+} greatly quenches the bandedge emission, while yields a broad band in the near infrared (NIR) region (Figure 12b).[110] Lowering the temperature

further favors the broad emission and red-shifts the emission peak (Figure 12c), similar to distorted 2D LHPs in which the broadband emission arises from the self-trapped exciton (STE).[111, 112] The ultrabroad emission is attributed to the luminescent center induced by interaction between distorted octahedra and spatially localized bipolarons (Figure 12d and e).[110] Similar broad emission is also observed in Bi^{3+}-doped $CsPbI_3$ NCs, suggesting the potential applications in the secondary biological window.[113]

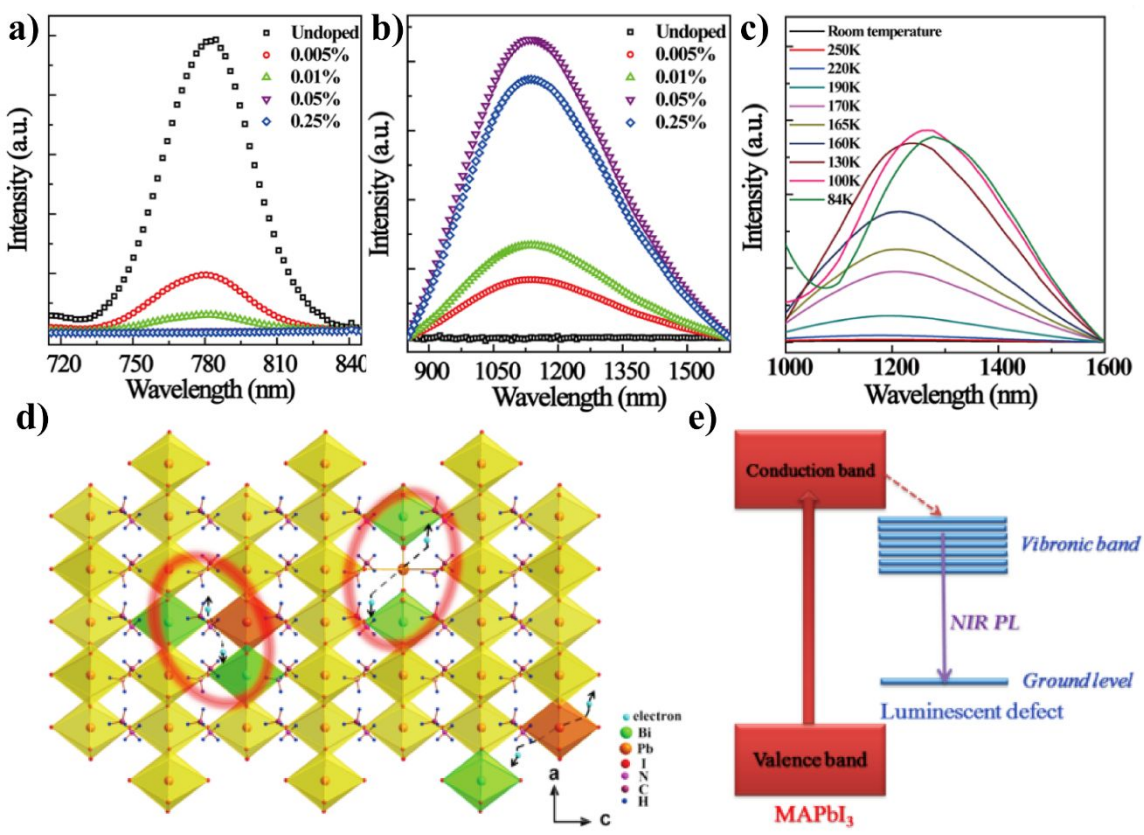

Figure 12. (a) and (b) PL spectra of the pristine and Bi^{3+}-doped $MAPbI_3$ films under the excitation of 517 nm. (c) Temperature-dependent NIR PL for the 0.05% film under the excitation of 517 nm. (d) Three-dimensional schematic illustration of the feasible structure of Bi^{3+}-doped $MAPbI_3$. The units in the red ellipses represent the proposed NIR luminescent centers. (e) Schematic energy diagram of the

Bi^{3+}-doped $MAPbI_3$. Adapted with permission from ref 110. Copyright 2016 American Chemical Society.

Compared to LHPs single crystals, Bi^{3+} doping has different impacts on the band alignment of $CsPbBr_3$ NCs.[39] Although the PL intensity of Bi^{3+}-doped $CsPbBr_3$ NCs shows similar tendency to that in I-based LHPs, the first excitonic absorption peak shifts to a lower energy at low doping level, while shifts to a higher energy at higher doping level (Figure 13a and b). Moreover, no evident Urbach tailing absorption is present, unlike that of Bi^{3+}-doped LHPs single crystals. Since dopant-induced states form a bandlike structure within the bandgap of the host with increasing dopant level, the abnormal spectral shift is attributed to the filling of the CB with extra electrons donated by dopants, known as the Burtein-Moss effect (Figure 13c).[114] By comparing the TA data (Figure 13d and e), the recovery time of the ground-state bleaching increases from 7 ns for undoped $CsPbBr_3$ NCs to 36 ns for 0.8% doped NCs, implying that the involvement of change in the electronic band structure delays carrier recombination in Bi^{3+}-doped $CsPbBr_3$ NCs. The reduced PL lifetime for Bi^{3+}-doped NCs further substantiates the presence of a high density of trap states.[39]

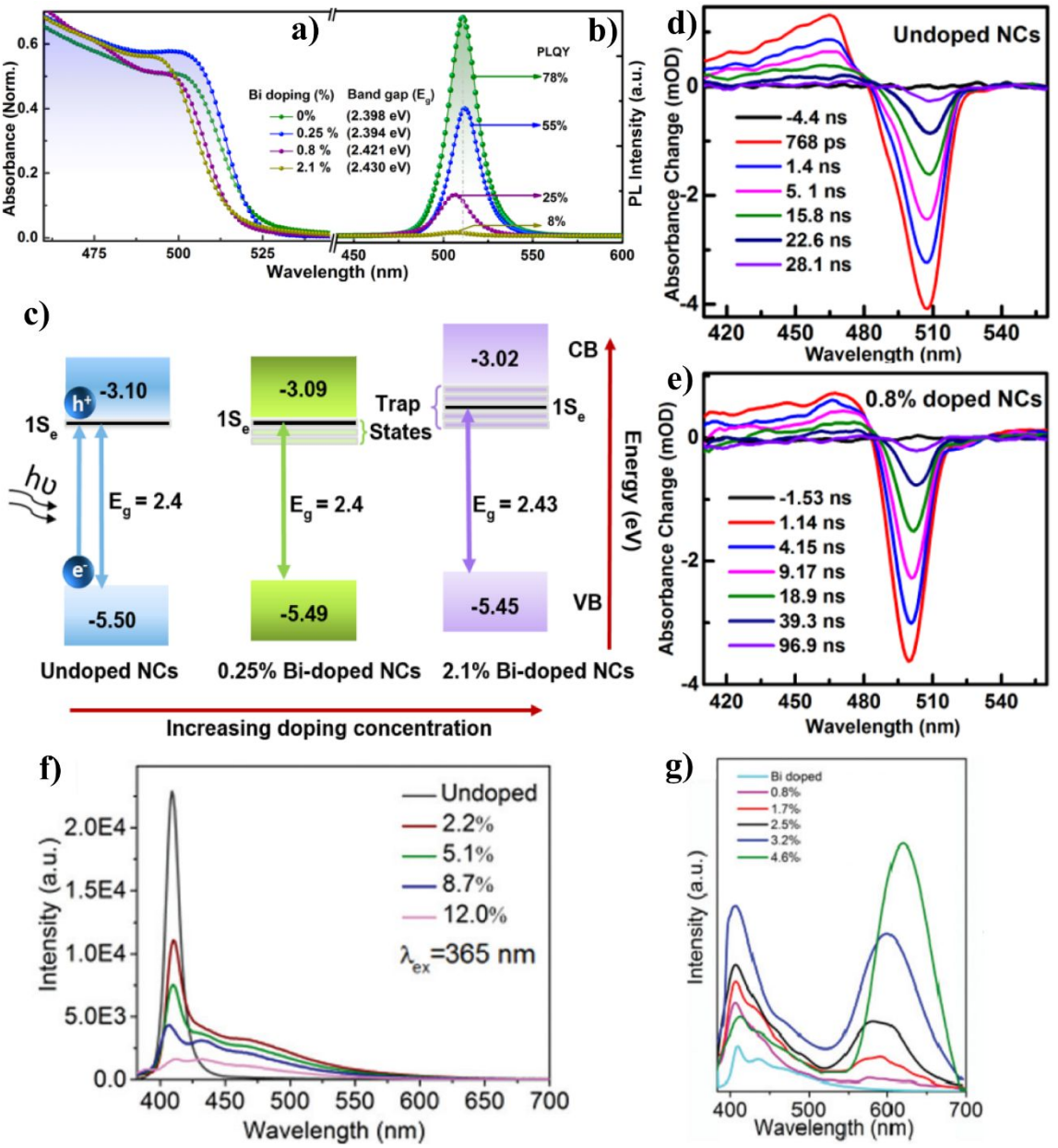

Figure 13.(a) Absorption and (b) PL spectra (λ_{ex} = 365 nm) of undoped and Bi^{3+}-doped (0.25%, 0.8%, and 2.1%) $CsPbBr_3$ NCs showing the spectral shift and change in the bandgap energy, E_g (calculated from a Tauc plot). ns-TA spectra at indicated delay times after 370 nm optical excitation of (c) $CsPbBr_3$ NCs and (d) 0.8% Bi^{3+}-doped $CsPbBr_3$ NCs in toluene. (f) PL spectra of undoped $CsPbCl_3$ NCs and Bi^{3+}-doped NCs with different doping concentrations in toluene solution. (g) PL spectra of Bi^{3+}-doped and codoped $CsPbCl_3$ NCs with 8.7% Bi^{3+} ions and different Mn^{2+} ion doping concentrations under 365

nm excitation. Adapted with permission from ref 39. Copyright 2017 American Chemical Society. Adapted with permission from ref 48. Copyright 2018 Royal Society of Chemistry.

Bi^{3+}-doped LHPs may be used for white light applications if the broad band induced by Bi^{3+} is located in the visible region. To explore this idea, Bi^{3+} has been successfully doped into $CsPbCl_3$ NCs to extend the emission into the visible (Figure 13f).[48] Along with the excitonic emission located at 410 nm, another broad band from 420 to 520 nm is observed for doped NCs, which is attributed to the intrinsic transitions ($^3P_1$–$^1S_0$) of Bi^{3+} ions.[48] To achieve white light emission, a yellow component is obtained by co-doping Mn^{2+} in Bi^{3+}-doped $CsPbCl_3$ NCs (Figure 13g). Additionally, both Bi^{3+} and Ag^+ are successfully co-doped in the LHPs to tailor the optical properties and band structure.[115] The doped products maintain a direct bandgap structure for the low alloying levels, with the reduced bandgap due to the combination of VBM increase induced by the Ag 4d orbital and CBM decrease induced by the Sb 5p or Bi 6p orbitals based on the DFT simulation results.

3.2.2 Rare earth doping. Rare earth elements, mainly lanthanides, are characterized by a partially filled 4f shell that is shielded from external field by $5s^2$ and $6p^6$ electrons.[116] As a result, their energy levels are not sensitive to the environment. Due to the parity forbiddance, the intra-4f transitions are partially allowed by crystal field interactions and opposite parity wavefunctions. Therefore, the luminescence lifetime of rare earth elements is extremely long (in the ms range) and linewidths are narrow.[116] Given the large absorption

cross section, weak electron-phonon coupling and very high internal PL QY, LHPs are suitable to be the host materials for the doping of rare earth elementals to achieve the downconversion, upconversion or quantum cutting application. Yb^{3+}/Ce^{3+} as well as Yb^{3+}/Er^{3+} codoped $CsPbCl_{1.5}Br_{1.5}$ PNCs have been synthesized and investigated in detail.[47] Besides the excitonic emission (450 nm) from the host, two other peaks at 488 and 988 nm are observed, attributed to the 4f-5d transition of Ce^{3+} and $^2F_{5/2}$–$^2F_{7/2}$ transition of Yb^{3+} ions, respectively (Figure 14a). By introducing Yb^{3+} and Ce^{3+} simultaneously, the overall PL QY is up to 146% resulting from the quantum cutting process, as verified by the almost doubled increase of Yb^{3+} emission intensity. The proposed mechanism of energy transfer is shown in Figure 14b, in which some electrons of the host generated by the 365 nm light relax to the energy level that is twice the level of Yb^{3+} ions, triggering the excitation of two electrons from $^2F_{7/2}$ to $^2F_{5/2}$. Upon codoping Ce^{3+} and Yb^{3+} ions into $CsPbCl_{1.5}Br_{1.5}$ NCs, the overall PL QY increases from 115.5% to 146%, associated with efficient energy transfer via a Ce^{3+} intermediate level.

Another study systematically examined the doping of various lanthanide ions (Ce^{3+}, Sm^{3+}, Eu^{3+}, Tb^{3+}, Dy^{3+}, Er^{3+}, and Yb^{3+}) into the lattice of $CsPbCl_3$ perovskite NCs.[31] The first excitonic absorption peak of host gradually shifts to red with decreasing atomic number of rare earth doping ions (Figure 14c), mainly attributed to the contraction of lattice and a small contribution from size decrease. Under the excitation of 365 nm light, the PL spectra of the doped LHP NCs show not only bandedge emission, but also several intense peaks (Figure 14d) associated with the electronic transitions of lanthanide ions: 4f−5d

transition for Ce^{3+}, $^4H_{5/2}$-^6H_J (J = 2/5, 2/7, 2/9, 2/11) for Sm^{3+}, $^5D_0$-^7F_J for Eu^{3+}, $^5D_4$-^7F_J (J = 3-6) for Tb^{3+}, $^4G_{5/2}$-^6H_J (J = 15/2, 13/2, 11/2) for Dy^{3+}, $^2H_{11/2}$-$^4I_{15/2}$/$^4S_{3/2}$-$^4I_{15/2}$ for E_r^{3+}, and $^2F_{5/2}$-$^2F_{7/2}$ for Yb^{3+} ions.

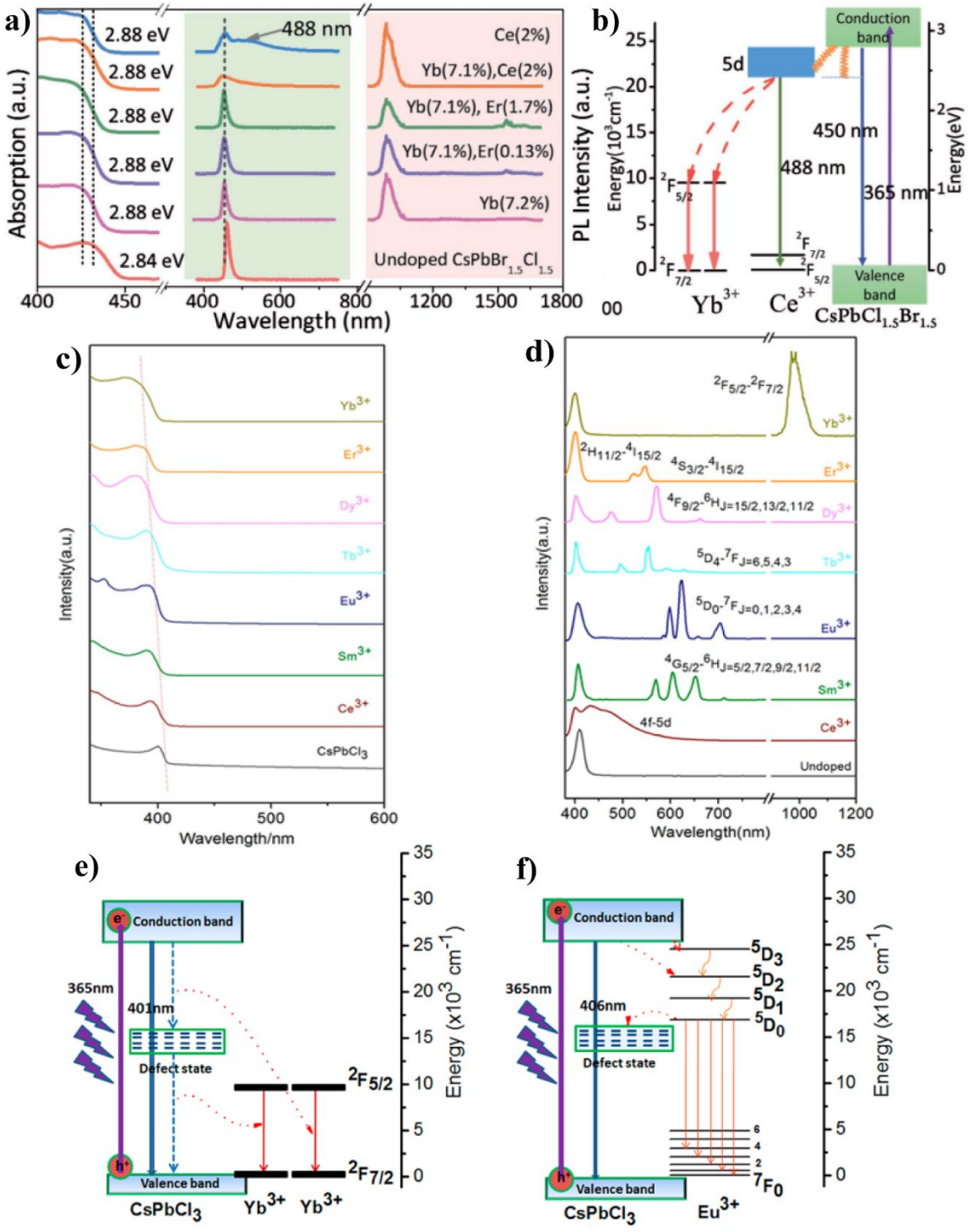

Figure 14. (a) Absorption (left), visible emission spectra (middle), and near-infrared emission spectra (right, excited by 365 nm light) of various Yb^{3+} ions doped perovskite QDs. (b) Absorption spectra (left), visible emission spectra (middle), and near-infrared emission spectra (right, excited by 365 nm

light) of $CsPbCl_{1.5}Br_{1.5}$ perovskite QDs codoping with different rare earth ions. (c) Absorption spectra and (d) emission spectra of $CsPbCl_3$ NCs doped with different lanthanide ions. (e) Energy level diagram of Yb^{3+}-doped $CsPbCl_3$ perovskite NCs and the possible quantum cutting mechanisms. (f) Energy level diagram of Eu^{3+}-doped $CsPbCl_3$ perovskite NCs and the possible PL mechanisms. Adapted with permission from ref 47. Copyright 2017 Wiley. Adapted with permission from ref 31. Copyright 2017 American Chemical Society.

Yb^{3+} doped $CsPbCl_3$ NCs exhibit a high PL QY of 143%, possibly resulting from the quantum cutting of excitonic transition.[31] As shown in Figure 14e, besides the excitonic recombination of the host, the electron in the CB can be transferred to a defect state accompanied by the excitation of one electron from $^2F_{7/2}$ to $^2F_{5/2}$. Subsequently, the electron in the intermediate defect state is further deactivated by recombining with VB hole and transfer its energy to another Yb^{3+} ion. As for Eu^{3+} doped NCs (Figure 14f), the excited electrons are transferred to the emitting level ($^5D_0$) nonradiatively, resulting in low PL QY.[31] Another detailed study revealed that the depopulation of the excitons of host in Yb^{3+} doped $CsPbCl_3$ NCs is extremely fast (ps time scale) as determined by TRPL and TA measurements (Figure 15a and b).[117] The possible explanation is that dopant-induced charge compensating defects act as shallow traps, competing with native defects and localizing the excitons on the ps time scale. For La^{3+} doped $CsPbCl_3$ NCs, the induced defects are slightly below the CB of the host (Figure 15c), resulting in near-bandedge PL. In the case of $CsPbCl_3$ NCs with Yb^{3+} dopant (Figure 15d), the charge-neutral Yb^{3+}-V_{Pb}-

Yb^{3+} defect complex (V_{Pb} denotes Pb vacancy, Figure 15e) traps the exciton followed by nearly resonant energy transfer to produce two excited Yb^{3+} ions in a single quantum-cutting step. With the aid of the V_{Pb} defect, the overall PL QY is up to 170%, which is the highest for any colloidal NCs and very close to the theoretical maximum 200%.

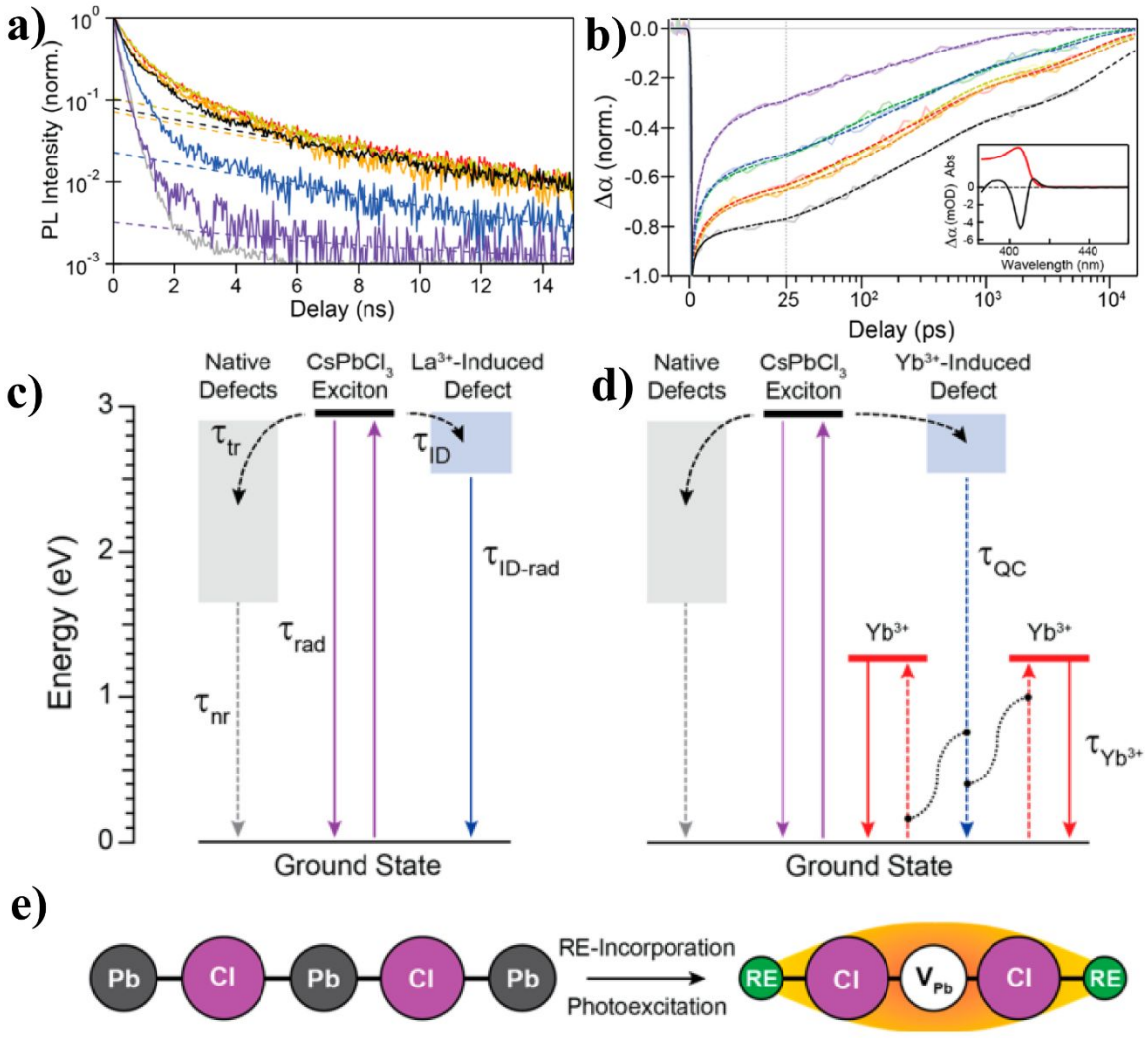

Figure 15. (a) Room-temperature TRPL decay traces for undoped (black trace) and Yb^{3+}-doped (red to purple) $CsPbCl_3$ NCs. The instrument response function (IRF) is also plotted (gray). The IRF curve is shifted downward by 10^{-3} for clarity of the logarithmic presentation. (b) First-exciton bleach-recovery kinetics measured at room temperature. Inset: representative absorption and transient-absorption spectra

at the $CsPbCl_3$ NC absorption edge showing the negative first-exciton bleach signal. (c) Proposed mechanism of La^{3+} induced defect emission process. (d) Yb^{3+} sensitization mechanism involving an analogous Yb^{3+}-induced defect states. (e) Proposed charge-neutral vacancy-defect structure arising from doping $CsPbCl_3$ NCs with trivalent cations. Adapted with permission from ref 117. Copyright 2018 American Chemical Society.

It is unavoidable that heterovalent doping induces defect states due to charge imbalance, which has a great impact on the exciton dynamics. Generally, defect states could trap photogenerated electrons/holes, leading to quenching of host PL. A contrary phenomenon was found in the case of Ce^{3+}-doped $CsPbBr_3$.[44] With the increase of dopant concentration, the overall PL was greatly enhanced with PL QY increased from 41% to 89% (Figure 16 a and b). Through TRPL and TA studies and global fitting of the dynamic data (Figure 16c and d for undoped sample, Figure 16e and f for doped sample), processes including intraband hot-exciton relaxation, exciton trapping to the bandgap trap states, and exciton recombination are identified. The former two decay processes are accelerated upon introducing Ce^{3+}. The induced near bandedge states result in the increased density of the lowest excitonic states and coupling between the higher excitonic energy levels and lowest excitonic states, as well as increased coupling between lowest excitonic states and the near bandedge trap states (Figure 16g).[44] In addition, since the induced near bandedge states are primarily emissive, its average PL lifetimes decrease gradually with increasing dopant

concentration (Figure 16h). Besides the aforementioned rare earth elements, Eu^{3+} and Tb^{3+} were also codoped into $CsPbBr_3$ NCs for white light application.[61]

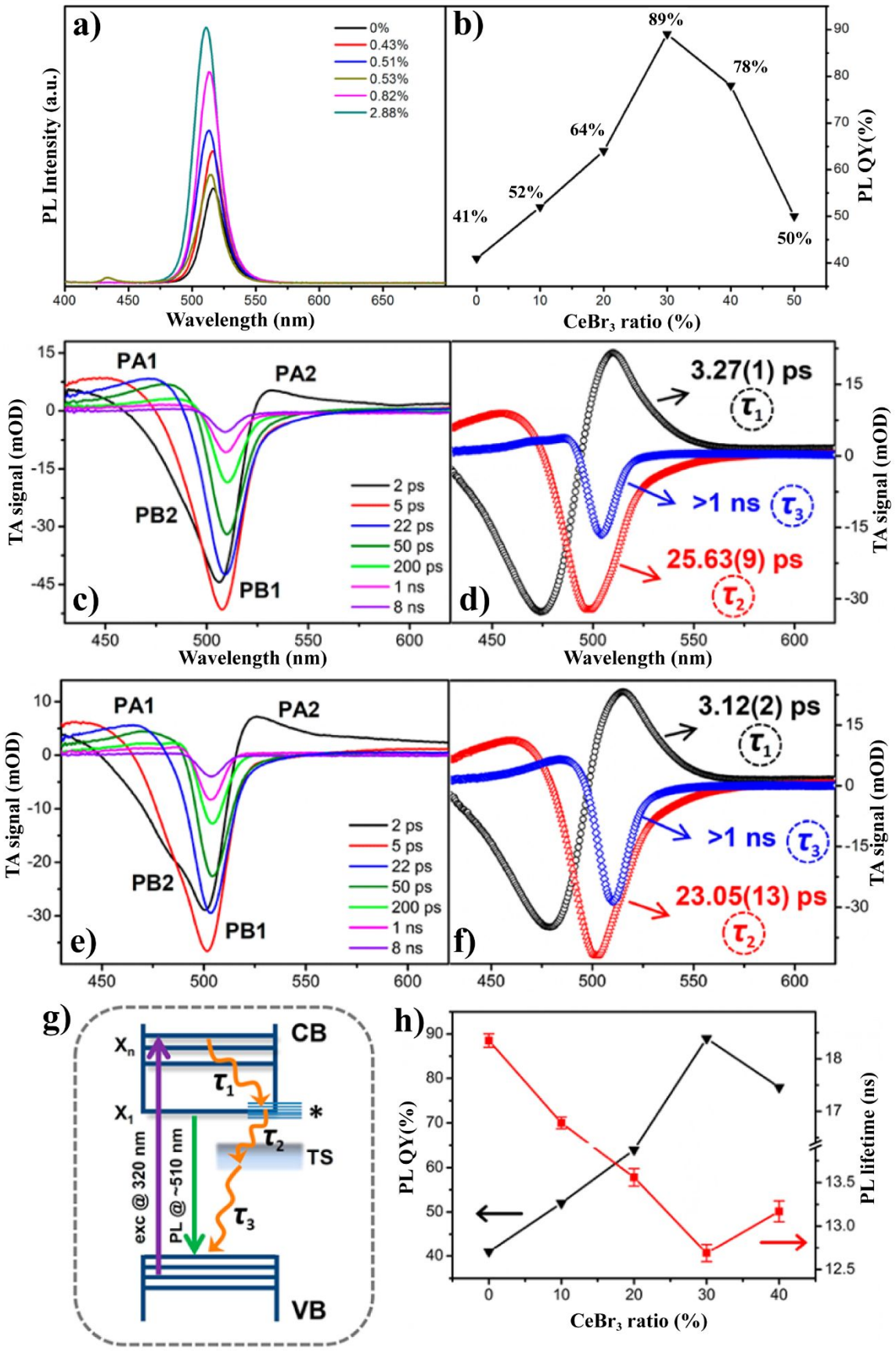
a)
PL Intensity (a.u.)
Wavelength (nm)
0%
0.43%
0.51%
0.53%
0.82%
2.88%
b)
89%
78%
64%
52%
41%
50%
PL QY(%)
CeBr3 ratio (%)
c)
PA1
PA2
PB2
PB1
2 ps
5 ps
22 ps
50 ps
200 ps
1 ns
8 ns
TA signal (mOD)
Wavelength (nm)
d)
3.27(1) ps
τ1
>1 ns
τ3
25.63(9) ps
τ2
e)
3.12(2) ps
23.05(13) ps
f)
g)
CB
Xn
X1
*
TS
VB
τ1
τ2
τ3
exc @ 320 nm
PL @ ~510 nm
h)
PL lifetime (ns)

Figure 16. (a) PL spectra (excitation at 365 nm) of undoped and doped $CsPbBr_3$ NCs with different Ce/Pb ratios. (b) PLQY versus dopant concentration of $CeBr_3$ (0-50%). (c) fs-TA spectra (excitation 320 nm) taken at several representative probe delays. (d) Decay-associated spectra for the undoped $CsPbBr_3$ NCs. (e) fs-TA spectra (excitation 320 nm) taken at several representative probe delays. (f) Decay-associated spectra for the doped $CsPbBr_3$ NCs. (g) Schematic illustration of the involved photophysical processes and mechanisms, where VB, CB, X_1, and X_n denote valence band, conduction band, the lowest excitonic state in the CB, and the higher-lying excitonic states in the CB, respectively. TS stands for the bandgap trap states, while the asterisk depicts the Ce^{3+}-doping induced states near the CB bandedge. (h) Trend comparison of the average PL lifetimes (red) and the PLQY results (black) versus the dopant concentration in terms of $CeBr_3$ ratio. Adapted with permission from ref 44. Copyright 2018 American Chemical Society.

A recent study on the upconversion luminescence (UCL) originated from the $CsPbX_3$ NCs is an example on the modification of the electronic properties of the doped perovskite NCs.[118] Fine tuning of the UCL in $CsPbX_3$ was achieved through sensitization by lanthanide-doped NCs, which is governed by a radiative energy transfer upconversion (RETU) process shown in Figure 17. Specifically, to sensitize photon upconversion in $CsPbX_3$ NCs, the NCs with different chemical compositions were dispersed with $LiYbF_4$:0.5%Tm^{3+}@$LiYF_4$ core/shell nanoparticles (NPs) in a homogeneous colloidal cyclohexane solution, in which the NPs can function as an internal UV or blue light source to illuminate the $CsPbX_3$ NCs by utilizing the intense UCL of Tm^{3+} under 980 nm CW

diode laser excitation. The characteristic bandedge excitonic emission from the $CsPbX_3$ NCs dominates in the UCL spectra, whereas the emissions of Tm^{3+} from the NPs were selectively quenched in accordance with the $CsPbX_3$ NC absorption, indicating efficient energy transfer from the NPs to $CsPbX_3$ NCs as CW laser cannot trigger photon upconversion in pure $CsPbX_3$ NCs (Figure 17a). The generality of the proposed RETU for sensitizing photon upconversion in $CsPbX_3$ NC has been also demonstrated. The UCL spectra for $LiYbF_4$:0.5%Tm^{3+}@$LiYF_4$ core/shell NPs, $NaYF_4$:18%Yb^{3+}, 2%Er^{3+} NPs, and the two kinds of NP-sensitized $CsPbX_3$ NCs are comparatively shown in Figure 17b and c, respectively.

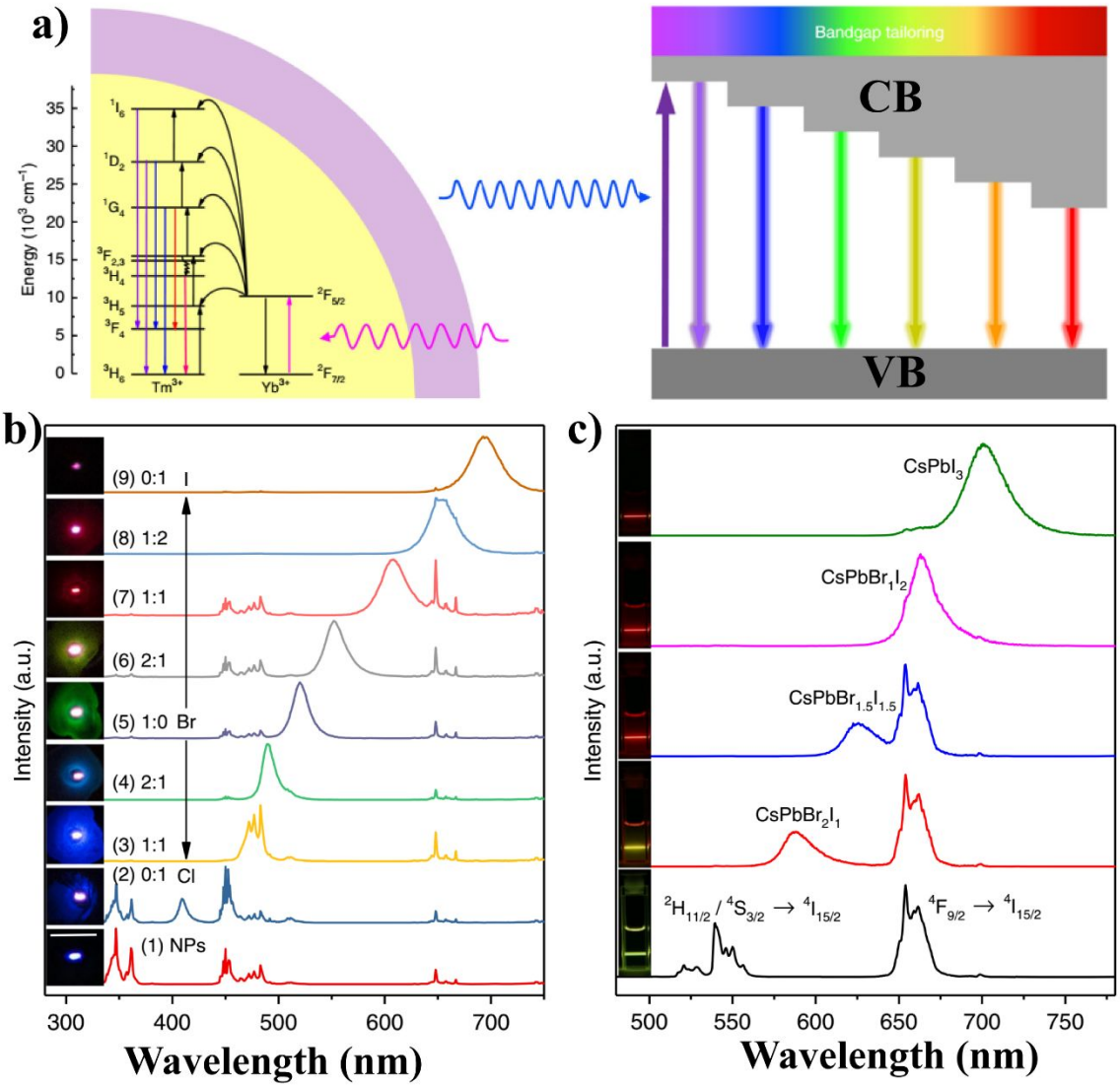

Figure 17. (a) Simplified energy-level scheme of $LiYbF_4$:0.5%Tm^{3+}@$LiYF_4$ core/shell NPs indicating major upconversion processes, and schematic illustration of full-color upconversion tuning in $CsPbX_3$ NCs through sensitization by the NPs. (b) UCL spectra for $LiYbF_4$:0.5%Tm^{3+}@$LiYF_4$ core/shell NPs and the NP-sensitized $CsPbX_3$ NCs with varying halide compositions under 980 nm CW diode laser excitation. (c) UCL spectra for $NaYF_4$:18%Yb^{3+}, 2%Er^{3+} NPs and the NP-sensitized $CsPbX_3$ NCs with varying halide composition under 980 nm CW diode laser excitation. The insets show the corresponding

UCL photographs for the colloidal cyclohexane solution of the NP-sensitized $CsPbX_3$ NCs. Adapted with permission from ref 118. Copyright 2018 Springer Nature.

3.2.3 Other heterovalent ions doping. Besides isovalent transition metal ions, other heterovalent ions such as Fe^{3+}, Al^{3+}, In^{3+} and Sb^{3+} have also been studied as dopant for LHPs.[32, 40, 119, 120] Uniform doping of Fe^{3+} in 1D $CsPb(Cl/Br)_3$ nanowires (NWs) has been reported, which is usually hard to achieve in both cross and longitudinal direction.[32] Both the growth process and optical properties of $CsPb(Cl/Br)_3$ NWs are strongly affected by $FeCl_3$ dopant (Figure 18a). The blue-shift of emission peak is attributed to the magnetic polaron, rather than the introduction of Cl. The PL lifetime of Fe-doped $CsPb(Cl/Br)_3$ NWs is much shorter than that of undoped $CsPbBr_3$ (Figure 18b), attributed to multiparticle effect (such as Auger recombination) facilitated by the increase of charge carrier density upon Fe^{3+} doping. In addition, Fe^{3+}-doped $CsPb(Cl/Br)_3$ NWs show high nonlinear absorption coefficient and high-quality optical properties, promising for optical switching applications.

As one of the earth-abundant elements, Al^{3+} has been used to dope $CsPbBr_3$ NCs, causing a major change in optical properties.[40] Both the absorption peak and emission band blue shift over 75 nm (Figure 18c and d), along with a decrease in PL QY upon Al^{3+} doping. The changes are attributed to the electronic doping by Al^{3+} ions and enhanced quantum confinement of NPs induced by the decrease of NP size. Compared to undoped samples, the shorter PL lifetime of Al^{3+}-doped samples is ascribed to the transfer of energy from the

host to Al^{3+} (Figure 18e). The dimeric form of Al_2Br_6 consisting of two $AlBr_4$ tetrahedral with shared edge is proposed to be dominant in the solid state (Figure 18f). However, the blue shift of PL was not observed in $MAPbI_3$ films (Figure 18g).[119] On the contrary, the average PL lifetime as well as PL QY of Al^{3+}-doped sample has an almost two-fold increase due to the higher quality of perovskite film and reduction of defect density (Figure 18h and i). Similar results were also observed in In^{3+}-doped $CH_3NH_3PbI_xCl_{3-x}$, in which the introduction of In and Cl affects the crystallization process and changes the crystallization orientation.[120] As an effective way to altering the type of semiconductor, heterovalent doping is also versatile for LHPs.

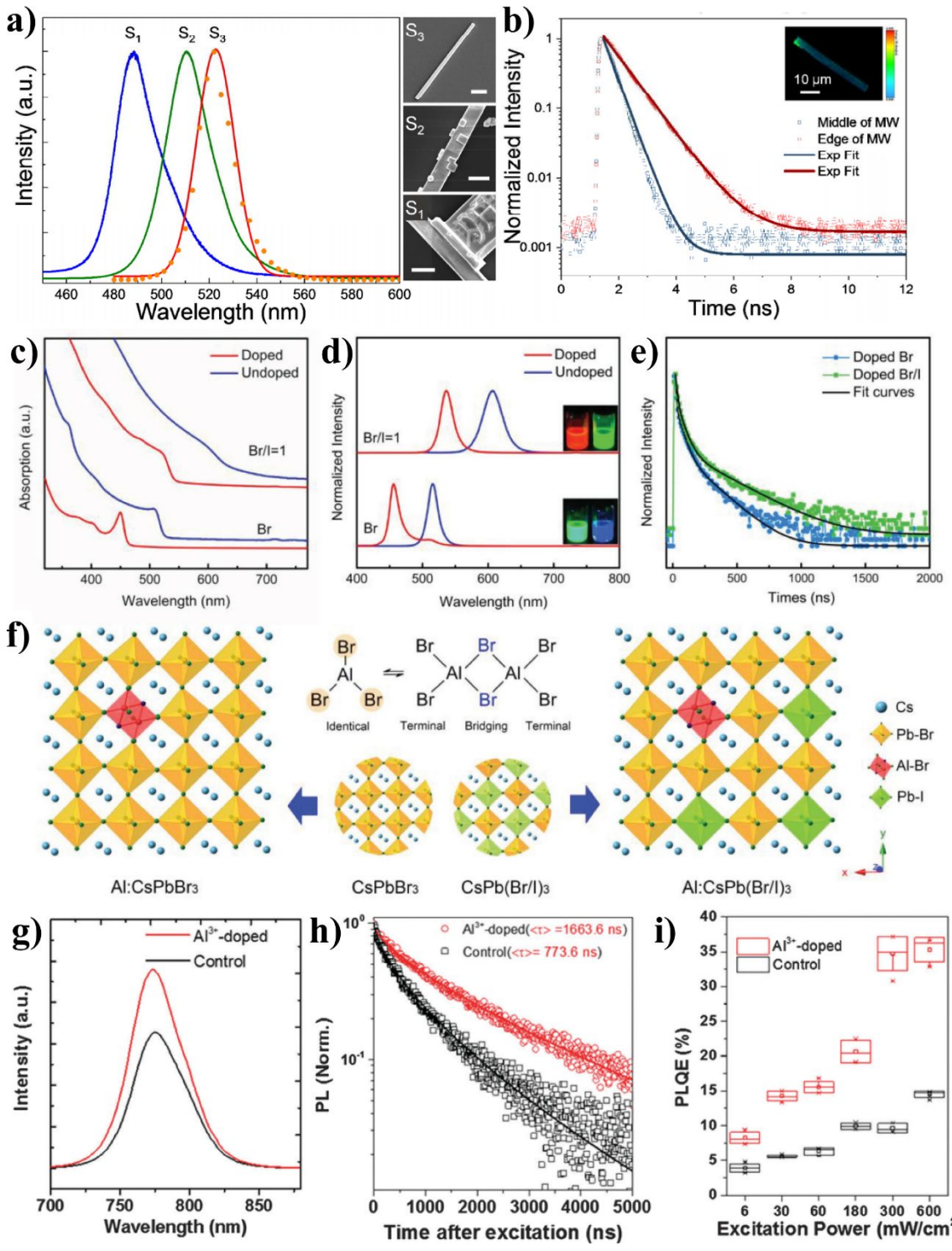

Figure 18. (a) PL spectra of varied Fe^{3+}-doped perovskite microstructures and the representative SEM images corresponding to the PL spectra (scale bar, 20 μm). (S_1, S_2 and S_3 represent different Fe elemental doping concentrations of S_1 = 2.34%, S_2 = 0.67%, S_3 = 0.48%). (b) PL dynamics under

different position excitation of Fe^{3+}-doped microwires. Solid line is single exponential fitting of the TRPL decay curve. (c) Absorption spectra of Al-doped and undoped $CsPbBr_3$ and $CsPb(Br/I)_3$ NCs. d) PL of Al^{3+}-doped and undoped $CsPbBr_3$ and $CsPb(Br/I)_3$ NCs. Insets are photographs of the sample under UV excitation. (e) Time-dependent Al luminescence intensity from Al^{3+}-doped $CsPbBr_3$ and $CsPb(Br/I)_3$ NCs. (f) Schematics showing the Al bound to host lattice constituents in cluster form. (g) PL spectroscopy of control (non-doped) and 0.15 mol% Al^{3+}-doped perovskite thin films deposited on glass substrate. (h) Time-resolved PL decay after excitation at 507 nm with pulsed (200 kHz) and a fluence of 30 nJ cm^{-2} per pulse. (i) PL quantum efficiency as a function of excitation power. Adapted with permission from ref 32. Copyright 2018 American Chemical Society. Adapted with permission from ref 40. Copyright 2017 Wiley. Adapted with permission from ref 119. Copyright 2017 Royal Society of Chemistry.

4. LIGHT EMISSION APPLICATIONS

4.1 LEDs application

For while light LED applications, it is desirable but difficult to obtain solid-state lighting materials with strong yellow or orange emission. $CsPbX_3$ NCs with mixed halide contents (*e.g.*, $CsPbCl_xBr_{3-x}$ and $CsPbBr_{3-x}I_x$) show low PLQY and stability due to phase separation. Doped LHPs, mostly the Mn^{2+}-doped $CsPbX_3$ NCs, can function well as efficient light emitters in perovskite light-emitting diodes (PLEDs) with higher maximum luminance, external quantum efficiency (EQE), and current efficiency (CE) when compared with the LEDs based on pure $CsPbX_3$ NCs.[91 121]

Pristine and doped $CsPbX_3$ NCs can be used for both PL and electroluminescence (EL) devices. For example, $CsPb_xMn_{1-x}Cl_3$ NCs-based LED device (Figure 19a and b) has been demonstrated with luminous efficiency of 2.2 lm/W and good stability under constant voltage of 3.5 V for 200 h.[42] Similarly, $CsPbBr_3$:Mn NCs have been utilized in PLEDs,[100] with a multilayer-structured architecture as illustrated in Figure 19c. Based on high quality $CsPbX_3$:Mn^{2+} NCs with good thermal and air stability, a series of PLEDs shows higher maximum luminance (9971 cd/m^2), enhanced EQE and CE than devices using pristine $CsPbX_3$ NCs (Figure 19d and e).

The thermostability of $CsPbX_3$ NCs is critical for LED device. For example, $CsPbCl_3$:Mn^{2+} NCs have been encapsulated in different matrixes such as KCl and polystyrene (PS) to improve their photostability and thermostability, and the resulting samples, $CsPbCl_3$:Mn^{2+}@KCl, $CsPbCl_3$:Mn^{2+}@PS, and $CsPbCl_3$:Mn^{2+} NCs, have been used in LEDs.[56] $CsPbCl_3$:Mn^{2+}@KCl exhibited greater photostability as well as thermostability compared to $CsPbCl_3$:Mn^{2+}@PS and $CsPbCl_3$:Mn^{2+} NCs. As a result, $CsPbCl_3$:Mn^{2+}@KCl tablet was adopted as a color converter in the LED coupled with a 365 nm GaN LED chip (Figure 19f). After continuously working at a voltage of 3 V for 100 h, the intensity of the LED remained 83% of initial value. Similarly, silica-coating is often applied to improve air stability of NCs, which can suppress the loss of Mn^{2+} and avoid anion exchange. Based on the PL color of the pure and doped $CsPbX_3$ NCs, light-emitting devices have been constructed by coupling green $CsPbBr_3$@SiO_2 and orange $CsPb_{0.835}Mn_{0.165}(Cl_{0.5}Br_{0.5})_3$@$SiO_2$ phosphors with an InGaN chip. The ratios of

$CsPbBr_3@SiO_2$ to $CsPb_{0.835}Mn_{0.165}(Cl_{0.5}Br_{0.5})_3@SiO_2$ can be used to finely tune color coordinates (CCT 5942~6636 K) and CRI (82.7-84.6) for the designed NCs-based white LEDs (Figure 19g). Importantly, no significant degradation or change of PL spectra was found, and the CRI, CCT as well as color coordinates were also stable with prolonging working time to 24 h, verifying the superior color stability for the constructed LHP $QDs@SiO_2$-based WLED.[88]

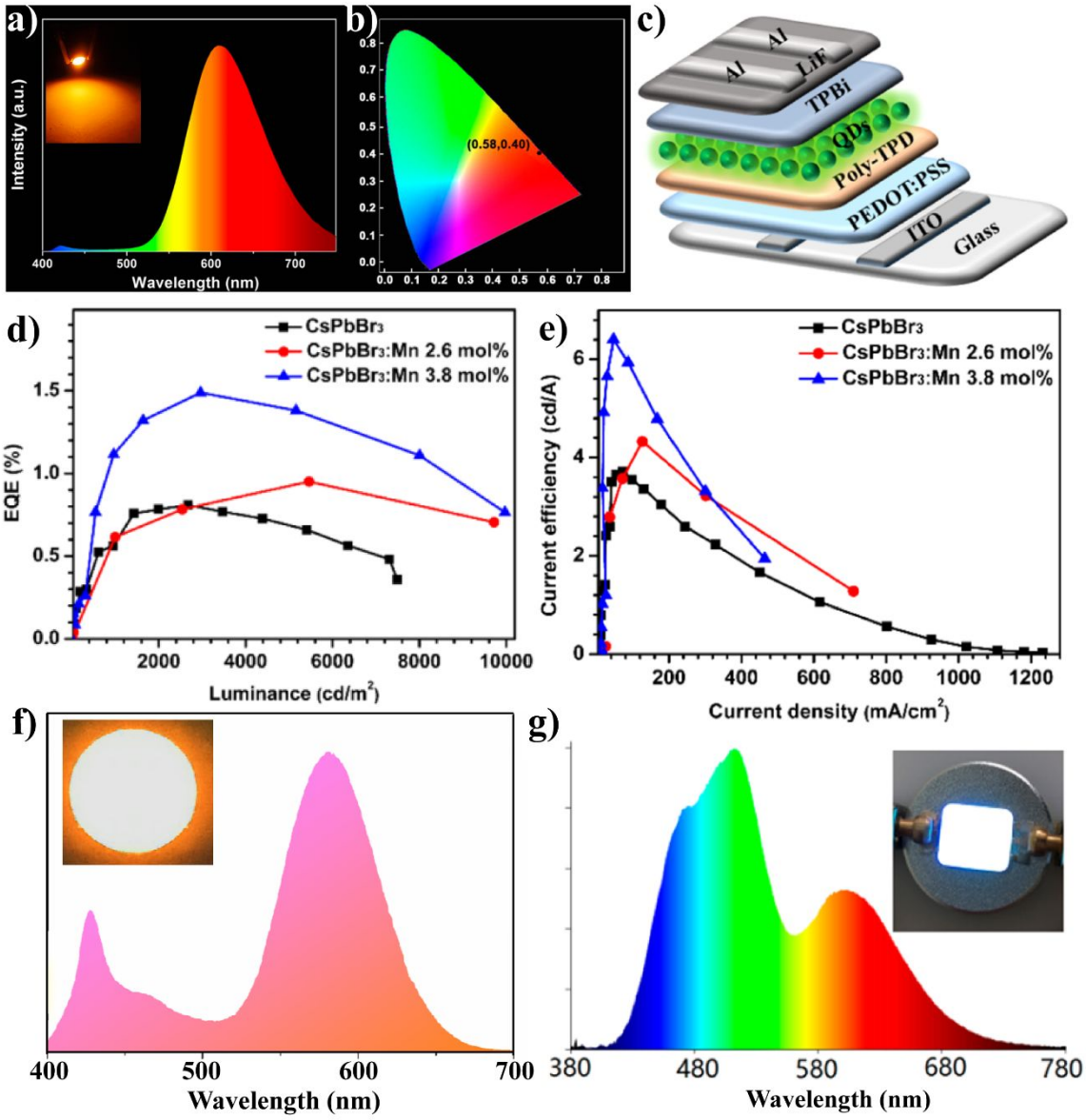

Figure 19. PL emission spectrum (a) and CIE chromaticity coordinate (b) of the as-fabricated LED from $CsPb_xMn_{1-x}Cl_3$ NCs. Inset of (a) is the optical image of the LED. (c) Schematic illustration of a typical multilayer-structured PLED device by using pure $CsPbBr_3$ and $CsPbBr_3$:Mn^{2+} (2.6 mol %) and $CsPbBr_3$:Mn^{2+} (3.8 mol %) NCs as green light emitters. (d) EQE of the devices as a function of luminance and (e) current efficiency as a function of current density. (f) Optical spectrum of $CsPbCl_3$:Mn^{2+}@KCl based LED. The inset of (f) is the scheme prototype and the optical image of the LED. (g) Electroluminescence spectrum of the designed light-emitting devices with green $CsPbBr_3$@SiO_2 and orange Mn^{2+}-doped $CsPb(Cl_{0.5}Br_{0.5})_3$@SiO_2 phosphors coated on the commercial InGaN blue chip. Inset of (g) is the corresponding white-light-emitting photograph for the constructed PQD@SiO_2-based device driven by 20 mA forward current. Adapted with permission from ref 42. Copyright 2017 American Chemical Society. Adapted with permission from ref 100. Copyright 2017 American Chemical Society. Adapted with permission from ref 56. Copyright 2017 Wiley. Adapted with permission from ref 88. Copyright 2017 American Chemical Society.

However, despite these achievements, the stability is still a challenging problem and future work is needed to improve the performance. For example, the Mn^{2+}-doped NCs severely suffer from photooxidation. Simple approaches to produce doped NCs with enhanced stability are highly desired.

4.2 Other applications

Doped LHPs are also promising for solar cell applications. For example,Yb^{3+}/Ce^{3+}

codoped $CsPbCl_{1.5}Br_{1.5}$ perovskite NC film self-assembled in front of the commercial silicon solar cells (SSCs) leads to enhanced photoelectric conversion efficiency (PCE) from 18.1% to 21.5% and excellent photostability (Figure 20a and b).[47] Similar work was also conducted on Mn^{2+} doped $CsPbCl_3$ NCs, in which $CsPbCl_3$:Mn^{2+}-based QDs serve as the energy-down-shift layer to boost the stability and efficiency of perovskite SCs (Figure 20c).[101]

Because of their sensitive response to the external environment, doped LHPs have also been used to construct temperature sensors. For instance, dually emitting Mn^{2+}-doped $CsPb(Cl/Br)_3$ NCs were used as the ratiometric temperature sensor due to the temperature-dependent exciton-to-Mn^{2+} energy transfer (Figure 20d).[55] The temperature-sensing is based on determination of the red-shift and quenching of the intrinsic PL emission of perovskite NCs as well as blue-shift and PL enhancing of the Mn^{2+} emission with the increasing temperature. Additionally, the optoelectronic applications of some representative doped LHPs are summarized in Table 1. These results suggest the great potential of doped LHPs not only in PVs and LEDs, but also in photodetectors, two-photo absorption and gas sensors.

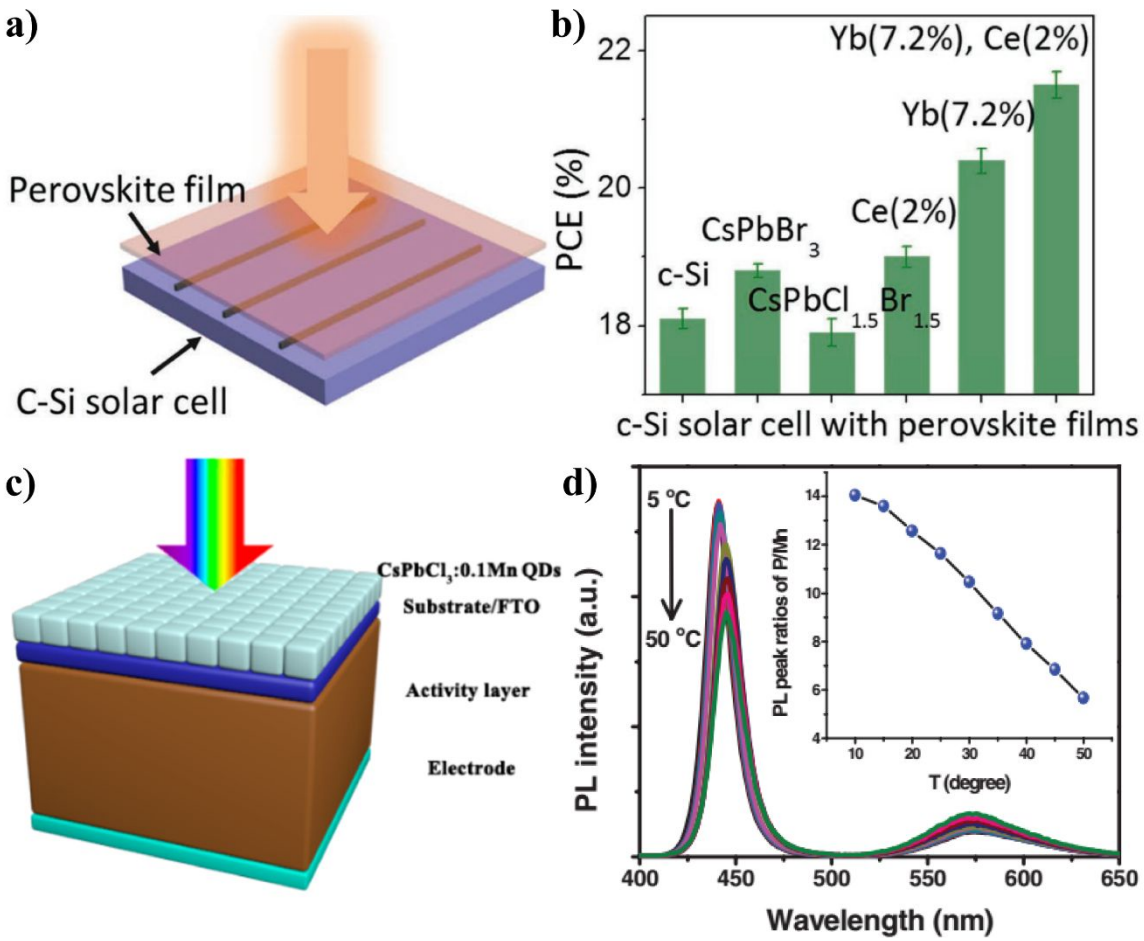

Figure 20. Schematic diagram of perovskite film to enhance the PCE of crystalline-silicon solar cells (a) and (b) PCE of SSCs coated with different perovskite NCs (b). Left to right: $CsPbBr_3$, $CsPbCl_{1.5}Br_{1.5}$, $CsPbCl_{1.5}Br_{1.5}$:Ce^{3+} (2%), $CsPbCl_{1.5}Br_{1.5}$:Yb^{3+} (7.1%), $CsPbCl_{1.5}Br_{1.5}$:Yb^{3+} (7.1%), Ce^{3+} (2%). (c) Schematic structure of solar cells coated with $CsPbCl_3$:0.1Mn^{2+} layer. (d) PL spectra of Mn^{2+}-doped $CsPbBr_3$ NCs collected from 5 to 50 ℃. The inset of (d) is PL peak intensity ratios between perovskite intrinsic emission and Mn^{2+} emission. Adapted with permission from ref 47. Copyright 2017 Wiley. Adapted with permission from ref 101. Copyright 2017 American Chemical Society. Adapted with permission from ref 55. Copyright 2017 Wiley.

Table 1 Summary of the applications of some representative doped LHPs

Host	Dopant	Synthesis strategy	Application	Performance	Reference
$MAPbI_3$	Ba^{2+}	Spin coating	Solar Cell	PCE = 17.4%; FF = 0.74; J_{sc} = 23 mA cm^{-2}; V_{oc} = 1.02 V	86
$MAPbI_3$	Sr^{2+}	Spin coating	Solar Cell	PCE = 15%; FF = 0.85; J_{sc} = 17.5 mA cm^{-2}; V_{oc} = 0.95 V	85
$CsPbBr_3$	Sn^{2+}	Hot-injection	LEDs	CE = 3.6 cd A^{-1}; EQE = N/A; Luminance = 5495 cd m^{-2}	79
$CsPbI_3$	Sn^{2+}	Solvothermal method	Photodetectors	Responsivity = 1.18 A W^{-1}; Detectivity = 6.43 × 10^{13} Jones;	64
$CsPbCl_3$	Ni^{2+}	Hot-injection	Violet Luminescence	PL QY = near unity	46
$CsPbCl_3$	Mn^{2+}	Hot-injection	O_2 sensor	Response time ≈ 5 s; linear range (0 ~ 12%)	89
$MAPbI_{3-x}Cl_x$	In^{3+}	Spin coating	Solar Cell	PCE = 17.55%; FF = 0.78 J_{sc} = 21.90 mA cm^{-2}; V_{oc} = 1.03 V	120
$CsPbBr_3$	Al^{3+}	Hot-injection	WLED	116% NTSC;[a] color coordinates (0.32, 0.34);	40
$CsPbBr_3$	Bi^{3+}	antisolvent vapour-assisted crystallization	Photostriction	Photostriction = 8 × 10^{-4}; Photostriction coefficient = 8 × 10^{-7} m^2 W^{-1}	65
$CsPb(Cl/Br)_3$	Fe^{3+}	Anti-solvent vapour-assisted crystallization	Two-photo absorption	Nonlinear absorption coefficient: ~210 cm/GW	32
$CsPbCl_3$	Yb^{3+}	Hot-injection	Quantum cutting	PL QY = 170%	117
$CsPbBr_3$	Ce^{3+}	Hot-injection	LED	CE = 14.2 cd A^{-1}; EQE = 4.4% (at 3.8 V)	44

Note that J_{sc}, short-circuit current; V_{oc}, open-circuit voltage; FF, fill factor.

[a] Al^{3+}-doped LHPs are combined with green $CsPbBr_3$ NCs and red-emitting CdSe@ZnS NCs for WLED

performance test.

5 CONCLUSION AND FUTURE PROSPECTS

In this article, we have reviewed recent developments on B-site doped LHPs, using isovalent ions such as alkaline-earth metals, transition metals and heterovalent ions including rare-earth metals, some main group metals, with an emphasis on understanding the effect of doping on the electronic band structure and energy or charge transfer processes. The synthetic routes for doped LHPs are also discussed to illustrate how to control the doping level and achieve co-doping. Through dopant engineering, the structural, morphological, optical and electronic properties of the LHPs host are varied and tailored towards diverse optoelectronic applications.

Despite the encouraging progress, however, the understanding on the doping mechanism, local environment of dopant ions, and dopant-host interaction is still very limited for B-site doped LHPs. Also, the underlying mechanisms of different synthesis approaches and variation of bandgap structure with doping remain unclear in most cases. For instance, one of the puzzling questions concerns the enlargement of bandgap induced by lattice contraction upon doping with smaller metal ions such as Sn^{2+}, Zn^{2+}, and Cd^{2+}, which is contradictory with the anti-bonding nature of energy band of LHPs. Therefore, better characterization of local environment of dopants is needed to understand the change of host lattice caused by dopants. In addition, the energy/electron transfer processes between host and dopants remain elusive in many systems. To achieve the desired optical properties, the interactions between host and dopants should be better understood, *e.g.* through time-

resolved studies such as fs TA and TRPL, as well as computational works.

Finally, instability of the LHPs is another major challenge to overcome. Recently, doped lead-free double perovskite shows not only impressive optical properties, but also improved thermal and moisture stability.[122, 123] These studies suggest the potential of developing lead-free double perovskites with different B-site cations to improve the intrinsic stability of the host and optical properties of the doped LHPs. Appropriate surface passivation is another possible approach to enhance stability of LHPs.[11, 16]

CONFLICTS OF INTEREST

There are no conflicts to declare.

ACKNOWLEDGEMENTS

This project was supported by NASA through the MACES Center at UC Merced (NNX15AQ01A), the BES Division of the US DOE, and UCSC Senate Special Research Fund. Work at the Molecular Foundry was supported by the Office of Science, Office of Basic Energy Sciences, the U.S. Department of Energy under Contract No. DE-AC02-05CH11231. B. L. thanks the support from National Natural Science Foundation of China (NSFC: 51702205) and STU Scientific Research Foundation for Talents (NTF17001).

REFERENCES

1. A. R. Chakhmouradian and P. M. Woodward, *Phys. Chem. Miner.*, 2014, 41, 387-391.
2. W. Li, Z. Wang, F. Deschler, S. Gao, R. H. Friend and A. K. Cheetham, *Nat. Rev. Mater.*, 2017, 2.
3. Jonathan Hwang, Reshma R. Rao, Livia Giordano, Yu Katayama, Yang Yu and Y. Shao-Horn, *Science*, 2017, 358, 751-756.
4. X. Xu, C. Su, W. Zhou, Y. Zhu, Y. Chen and Z. Shao, *Adv. Sci.*, 2016, 3, 1500187.
5. J. Sunarso, S. S. Hashim, N. Zhu and W. Zhou, *Prog. Energy Combust. Sci.*, 2017, 61, 57-77.
6. S. K. Tiwari, S. P. Singh and R. N. Singh, *J. Electrochem. Soc.*, 1996, 143, 1505-1510.
7. A. Kojima, K. Teshima, Y. Shirai and T. Miyasaka, *J. Am. Chem. Soc.*, 2009, 131, 6050-6051.
8. W. J. Yin, T. Shi and Y. Yan, *Adv. Mater.*, 2014, 26, 4653-4658.
9. B. Luo, S. B. Naghadeh and J. Z. Zhang, *ChemNanoMat*, 2017, 3, 456-465.
10. J. S. Manser, J. A. Christians and P. V. Kamat, *Chem. Rev.*, 2016, 116, 12956-13008.
11. S. Bonabi Naghadeh, B. Luo, G. Abdelmageed, Y.-C. Pu, C. Zhang and J. Z. Zhang, *J. Phys. Chem. C*, 2018, 122, 15799-15818.
12. B. Saparov and D. B. Mitzi, *Chem. Rev.*, 2016, 116, 4558-4596.
13. M. T. Klug, A. Osherov, A. A. Haghighirad, S. D. Stranks, P. R. Brown, S. Bai, J. T. W. Wang, X. Dang, V. Bulović, H. J. Snaith and A. M. Belcher, *Energy Environ. Sci.*, 2017, 10, 236-246.

14. S. Das Adhikari, S. K. Dutta, A. Dutta, A. K. Guria and N. Pradhan, *Angew. Chem. Int. Ed.*, 2017, 56, 8746-8750.

15. J. D. B. a. D. R. GAMELIN, *Prog. Inorg. Chem.*, 2005, 54, 47-126.

16. H. Huang, M. I. Bodnarchuk, S. V. Kershaw, M. V. Kovalenko and A. L. Rogach, *ACS Energy Lett.*, 2017, 2, 2071-2083.

17. Y. Shi, J. Xi, T. Lei, F. Yuan, J. Dai, C. Ran, H. Dong, B. Jiao, X. Hou and Z. Wu, *ACS Appl. Mater. Interfaces*, 2018, 10, 9849-9857.

18. Q. A. Akkerman, D. Meggiolaro, Z. Dang, F. De Angelis and L. Manna, *ACS Energy Lett.*, 2017, 2, 2183-2186.

19. Abhishek Swarnkar, Ashley R. Marshall, Erin M. Sanehira, Boris D. Chernomordik, David T. Moore, Jeffrey A. Christians, Tamoghna Chakrabarti and J. M. Luther, *Science*, 2016, 354, 92-95.

20. G. S. David P. McMeekin, Waqaas Rehman, Giles E. Eperon,, M. T. H. Michael Saliba, Amir Haghighirad, Nobuya Sakai, and B. R. Lars Korte, Michael B. Johnston, Laura M. Herz, Henry J. Snaith, *Science*, 2016, 351, 151-155.

21. H. Z. Feng Zhang, Cheng Chen, Xian-gang Wu, Xiangmin Hu, Hailong Huang, Junbo Han, Bingsuo Zou, and Yuping Dong, *ACS Nano*, 2015, 9, 4533-4542.

22. Y. Chen, B. Li, W. Huang, D. Gao and Z. Liang, *Chem. Commun.*, 2015, 51, 11997-11999.

23. M. K. Kim, T. Jeon, H. I. Park, J. M. Lee, S. A. Nam and S. O. Kim, *CrystEngComm*, 2016, 18, 6090-6095.

24. A. Halder, R. Chulliyil, A. S. Subbiah, T. Khan, S. Chattoraj, A. Chowdhury and S. K.

Sarkar, *J. Phys. Chem. Lett.*, 2015, 6, 3483-3489.

25. Z. Xiao, W. Meng, B. Saparov, H. S. Duan, C. Wang, C. Feng, W. Liao, W. Ke, D. Zhao, J. Wang, D. B. Mitzi and Y. Yan, *J. Phys. Chem. Lett.*, 2016, 7, 1213-1218.

26. Q. Tai, P. You, H. Sang, Z. Liu, C. Hu, H. L. Chan and F. Yan, *Nat. Commun.*, 2016, 7, 11105.

27. G. E. Eperon and D. S. Ginger, *ACS Energy Lett.*, 2017, 2, 1190-1196.

28. A. B. F. Vitoreti, S. Agouram, M. Solis de la Fuente, V. Munoz-Sanjose, M. A. Schiavon and I. Mora-Sero, *J. Phys. Chem. C*, 2018, 122, 14222-14231.

29. W. Liu, Q. Lin, H. Li, K. Wu, I. Robel, J. M. Pietryga and V. I. Klimov, *J. Am. Chem. Soc.*, 2016, 138, 14954-14961.

30. D. Parobek, B. J. Roman, Y. Dong, H. Jin, E. Lee, M. Sheldon and D. H. Son, *Nano Lett.*, 2016, 16, 7376-7380.

31. G. Pan, X. Bai, D. Yang, X. Chen, P. Jing, S. Qu, L. Zhang, D. Zhou, J. Zhu, W. Xu, B. Dong and H. Song, *Nano Lett.*, 2017, 17, 8005-8011.

32. S. Zou, G. Yang, T. Yang, D. Zhao, Z. Gan, W. Chen, H. Zhong, X. Wen, B. Jia and B. Zou, *J. Phys. Chem. Lett.*, 2018, 9, 4878-4885.

33. Y. Zhou, J. Chen, O. M. Bakr and H.-T. Sun, *Chem. Mater.*, 2018, 30, 6589-6613.

34. J. Zhang, Q. Di, J. Liu, B. Bai, J. Liu, M. Xu and J. Liu, *J. Phys. Chem. Lett.*, 2017, 8, 4943-4953.

35. R. Buonsanti and D. J. Milliron, *Chem. Mater.*, 2013, 25, 1305-1317.

36. S. D. A. Narayan Pradhan, Angshuman Nag, and D. D. Sarma, *Angew. Chem. Int. Ed.*, 2017,

56, 7038 – 7054.

37. L. Protesescu, S. Yakunin, M. I. Bodnarchuk, F. Krieg, R. Caputo, C. H. Hendon, R. X. Yang, A. Walsh and M. V. Kovalenko, *Nano Lett.*, 2015, 15, 3692-3696.

38. W. J. Mir, M. Jagadeeswararao, S. Das and A. Nag, *ACS Energy Lett.*, 2017, 2, 537-543.

39. R. Begum, M. R. Parida, A. L. Abdelhady, B. Murali, N. M. Alyami, G. H. Ahmed, M. N. Hedhili, O. M. Bakr and O. F. Mohammed, *J. Am. Chem. Soc.*, 2017, 139, 731-737.

40. M. Liu, G. Zhong, Y. Yin, J. Miao, K. Li, C. Wang, X. Xu, C. Shen and H. Meng, *Adv. Sci.*, 2017, 1700335.

41. X. Yuan, S. Ji, M. C. De Siena, L. Fei, Z. Zhao, Y. Wang, H. Li, J. Zhao and D. R. Gamelin, *Chem. Mater.*, 2017, 29, 8003-8011.

42. H. Liu, Z. Wu, J. Shao, D. Yao, H. Gao, Y. Liu, W. Yu, H. Zhang and B. Yang, *ACS Nano*, 2017, 11, 2239-2247.

43. A. De, N. Mondal and A. Samanta, *Nanoscale*, 2017, 9, 16722-16727.

44. J. S. Yao, J. Ge, B. N. Han, K. H. Wang, H. B. Yao, H. L. Yu, J. H. Li, B. S. Zhu, J. Z. Song, C. Chen, Q. Zhang, H. B. Zeng, Y. Luo and S. H. Yu, *J. Am. Chem. Soc.*, 2018, 140, 3626-3634.

45. H. C. Wang, W. Wang, A. C. Tang, H. Y. Tsai, Z. Bao, T. Ihara, N. Yarita, H. Tahara, Y. Kanemitsu, S. Chen and R. S. Liu, *Angew. Chem. Int. Ed.*, 2017, 56, 13650-13654.

46. Z. J. Yong, S. Q. Guo, J. P. Ma, J. Y. Zhang, Z. Y. Li, Y. M. Chen, B. B. Zhang, Y. Zhou, J. Shu, J. L. Gu, L. R. Zheng, O. M. Bakr and H. T. Sun, *J. Am. Chem. Soc.*, 2018, 140, 9942-9951.

47. D. Zhou, D. Liu, G. Pan, X. Chen, D. Li, W. Xu, X. Bai and H. Song, *Adv. Mater.*, 2017, 29.

48. H. Shao, X. Bai, H. Cui, G. Pan, P. Jing, S. Qu, J. Zhu, Y. Zhai, B. Dong and H. Song, *Nanoscale*, 2018, 10, 1023-1029.

49. C. Zhou, Y. Tian, O. Khabou, M. Worku, Y. Zhou, J. Hurley, H. Lin and B. Ma, *ACS Appl. Mater. Interfaces*, 2017, 9, 40446-40451.

50. X. Li, Y. Guo and B. Luo, *Crystals*, 2017, 8, 4.

51. Y. Yuan and J. Huang, *Acc. Chem. Res.*, 2016, 49, 286-293.

52. C. Eames, J. M. Frost, P. R. Barnes, B. C. O'Regan, A. Walsh and M. S. Islam, *Nat. Commun.*, 2015, 6, 7497.

53. G. Nedelcu, L. Protesescu, S. Yakunin, M. I. Bodnarchuk, M. J. Grotevent and M. V. Kovalenko, *Nano Lett.*, 2015, 15, 5635-5640.

54. W. van der Stam, J. J. Geuchies, T. Altantzis, K. H. van den Bos, J. D. Meeldijk, S. Van Aert, S. Bals, D. Vanmaekelbergh and C. de Mello Donega, *J. Am. Chem. Soc.*, 2017, 139, 4087-4097.

55. G. Huang, C. Wang, S. Xu, S. Zong, J. Lu, Z. Wang, C. Lu and Y. Cui, *Adv. Mater.*, 2017, 29.

56. W. Xu, F. Li, F. Lin, Y. Chen, Z. Cai, Y. Wang and X. Chen, *Adv. Opt. Mater.*, 2017, 5, 1700520.

57. M. Li, X. Zhang, K. Matras-Postolek, H.-S. Chen and P. Yang, *J. Mater. Chem. C*, 2018, 6, 5506-5513.

58. F. Li, Z. Xia, Y. Gong, L. Gu and Q. Liu, *J. Mater. Chem. C*, 2017, 5, 9281-9287.

59. B. Q. Di Gao, Zheng Xu, Dandan Song, Pengjie Song, Zhiqin Liang, Zhaohui Shen, Jingyue Cao, Junjie Zhang and Suling Zhao, *J. Phys. Chem. C*, 2017, 121, 20387-20395.

60. Q. Hu, Z. Li, Z. Tan, H. Song, C. Ge, G. Niu, J. Han and J. Tang, *Adv. Opt. Mater.*, 2018, 6, 1700864.

61. Y. Cheng, C. Shen, L. Shen, W. Xiang and X. Liang, *ACS Appl. Mater. Interfaces*, 2018, 10, 21434-21444.

62. S.-H. Chan, M.-C. Wu, K.-M. Lee, W.-C. Chen, T.-H. Lin and W.-F. Su, *J. Mater. Chem. A*, 2017, 5, 18044-18052.

63. C. F. J. Lau, M. Zhang, X. Deng, J. Zheng, J. Bing, Q. Ma, J. Kim, L. Hu, M. A. Green, S. Huang and A. Ho-Baillie, *ACS Energy Lett.*, 2017, 2, 2319-2325.

64. Z. Du, D. Fu, T. Yang, Z. Fang, W. Liu, F. Gao, L. Wang, Z. Yang, J. Teng, H. Zhang and W. Yang, *J. Mater. Chem. C*, 2018, 6, 6287-6296.

65. X. Miao, T. Qiu, S. Zhang, H. Ma, Y. Hu, F. Bai and Z. Wu, *J. Mater. Chem. C*, 2017, 5, 4931-4939.

66. Y. Yamada, M. Hoyano, R. Akashi, K. Oto and Y. Kanemitsu, *J. Phys. Chem. Lett.*, 2017, 8, 5798-5803.

67. Z. Zhang, L. Ren, H. Yan, S. Guo, S. Wang, M. Wang and K. Jin, *J. Phys. Chem. C*, 2017, 121, 17436-17441.

68. F. Hao, C. C. Stoumpos, R. P. Chang and M. G. Kanatzidis, *J. Am. Chem. Soc.*, 2014, 136, 8094-8099.

69. H. J. Feng, T. R. Paudel, E. Y. Tsymbal and X. C. Zeng, *J. Am. Chem. Soc.*, 2015, 137, 8227-

8236.

70. D. Zhao, Y. Yu, C. Wang, W. Liao, N. Shrestha, C. R. Grice, A. J. Cimaroli, L. Guan, R. J. Ellingson, K. Zhu, X. Zhao, R.-G. Xiong and Y. Yan, *Nat. Energy*, 2017, 2, 17018.

71. Y. Ogomi, A. Morita, S. Tsukamoto, T. Saitho, N. Fujikawa, Q. Shen, T. Toyoda, K. Yoshino, S. S. Pandey, T. Ma and S. Hayase, *J. Phys. Chem. Lett.*, 2014, 5, 1004-1011.

72. L. Vegard, *Zeitschrift für Physik*, 1921, 5, 17-26.

73. J. Im, C. C. Stoumpos, H. Jin, A. J. Freeman and M. G. Kanatzidis, *J. Phys. Chem. Lett.*, 2015, 6, 3503-3509.

74. A. Mancini, P. Quadrelli, C. Milanese, M. Patrini, G. Guizzetti and L. Malavasi, *Inorg. Chem.*, 2015, 54, 8893-8895.

75. D. Ju, Y. Dang, Z. Zhu, H. Liu, C.-C. Chueh, X. Li, L. Wang, X. Hu, A. K. Y. Jen and X. Tao, *Chem. Mater.*, 2018, 30, 1556-1565.

76. K. Wei, Z. Xu, R. Chen, X. Zheng, X. Cheng and T. Jiang, *Opt. Lett.*, 2016, 41, 3821-3824.

77. R. Prasanna, A. Gold-Parker, T. Leijtens, B. Conings, A. Babayigit, H. G. Boyen, M. F. Toney and M. D. McGehee, *J. Am. Chem. Soc.*, 2017, 139, 11117-11124.

78. J. Navas, A. Sanchez-Coronilla, J. J. Gallardo, N. C. Hernandez, J. C. Pinero, R. Alcantara, C. Fernandez-Lorenzo, D. M. De los Santos, T. Aguilar and J. Martin-Calleja, *Nanoscale*, 2015, 7, 6216-6229.

79. X. Zhang, W. Cao, W. Wang, B. Xu, S. Liu, H. Dai, S. Chen, K. Wang and X. W. Sun, *Nano Energy*, 2016, 30, 511-516.

80. M. R. Filip and F. Giustino, *J. Phys. Chem. C*, 2015, 120, 166-173.

81. M. Pazoki, T. J. Jacobsson, A. Hagfeldt, G. Boschloo and T. Edvinsson, *Phys. Rev. B*, 2016, 93.

82. T. J. Jacobsson, M. Pazoki, A. Hagfeldt and T. Edvinsson, *J. Phys. Chem. C*, 2015, 119, 25673-25683.

83. M.-C. Wu, T.-H. Lin, S.-H. Chan and W.-F. Su, *J. Taiwan Inst. Chem. E.*, 2017, 80, 695-700.

84. X. Shai, L. Zuo, P. Sun, P. Liao, W. Huang, E.-P. Yao, H. Li, S. Liu, Y. Shen, Y. Yang and M. Wang, *Nano Energy*, 2017, 36, 213-222.

85. D. Perez-Del-Rey, D. Forgacs, E. M. Hutter, T. J. Savenije, D. Nordlund, P. Schulz, J. J. Berry, M. Sessolo and H. J. Bolink, *Adv. Mater.*, 2016, 28, 9839-9845.

86. H. Zhang, M.-h. Shang, X. Zheng, Z. Zeng, R. Chen, Y. Zhang, J. Zhang and Y. Zhu, *Electrochim. Acta*, 2017, 254, 165-171.

87. N. Pradhan, *ChemPhysChem,* 2016, 17, 1087-1094.

88. D. Chen, G. Fang and X. Chen, *ACS Appl. Mater. Interfaces*, 2017, 9, 40477-40487.

89. F. Lin, F. Li, Z. Lai, Z. Cai, Y. Wang, O. S. Wolfbeis and X. Chen, *ACS Appl. Mater. Interfaces*, 2018, 10, 23335-23343.

90. A. K. Guria, S. K. Dutta, S. D. Adhikari and N. Pradhan, *ACS Energy Lett.*, 2017, 2, 1014-1021.

91. C. C. Lin, K. Y. Xu, D. Wang and A. Meijerink, *Sci. Rep.*, 2017, 7, 45906.

92. P. Wang, B. Dong, Z. Cui, R. Gao, G. Su, W. Wang and L. Cao, *RSC Adv.*, 2018, 8, 1940-1947.

93. M. H. P. Usman, R. Bakthavatsalam and J. Kundu, *ChemistrySelect*, 2018, 3, 6585-6595.

94. F. Wang, M. Yang, S. Ji, L. Yang, J. Zhao, H. Liu, Y. Sui, Y. Sun, J. Yang and X. Zhang, *J. Power Sources*, 2018, 395, 85-91.

95. S. Ye, J. Y. Sun, Y. H. Han, Y. Y. Zhou and Q. Y. Zhang, *ACS Appl. Mater. Interfaces*, 2018, 10, 24656-24664.

96. V. K. Ravi, G. B. Markad and A. Nag, *ACS Energy Lett.*, 2016, 1, 665-671.

97. D. Parobek, Y. Dong, T. Qiao and D. H. Son, *Chem. Mater.*, 2018, 30, 2939-2944.

98. A. Biswas, R. Bakthavatsalam and J. Kundu, *Chem. Mater.*, 2017, 29, 7816-7825.

99. D. Rossi, D. Parobek, Y. Dong and D. H. Son, *J. Phys. Chem. C*, 2017, 121, 17143-17149.

100. S. Zou, Y. Liu, J. Li, C. Liu, R. Feng, F. Jiang, Y. Li, J. Song, H. Zeng, M. Hong and X. Chen, *J. Am. Chem. Soc.*, 2017, 139, 11443-11450.

101. Q. Wang, X. Zhang, Z. Jin, J. Zhang, Z. Gao, Y. Li and S. F. Liu, *ACS Energy Lett.*, 2017, 2, 1479-1486.

102. Q. Wei, M. Li, Z. Zhang, J. Guo, G. Xing, T. C. Sum and W. Huang, *Nano Energy*, 2018, 51, 704-710.

103. J. Zhu, X. Yang, Y. Zhu, Y. Wang, J. Cai, J. Shen, L. Sun and C. Li, *J. Phys. Chem. Lett.*, 2017, 8, 4167-4171.

104. P. Arunkumar, K. H. Gil, S. Won, S. Unithrattil, Y. H. Kim, H. J. Kim and W. B. Im, *J. Phys. Chem. Lett.*, 2017, 8, 4161-4166.

105. W. Xu, L. Zheng, X. Zhang, Y. Cao, T. Meng, D. Wu, L. Liu, W. Hu and X. Gong, *Adv. Energy Mater.*, 2018, 8, 1703178.

106. A. L. Abdelhady, M. I. Saidaminov, B. Murali, V. Adinolfi, O. Voznyy, K. Katsiev, E.

Alarousu, R. Comin, I. Dursun, L. Sinatra, E. H. Sargent, O. F. Mohammed and O. M. Bakr, *J. Phys. Chem. Lett.*, 2016, 7, 295-301.

107. V. A. Dong Shi, Riccardo Comin, Mingjian Yuan, Erkki Alarousu, and Y. C. Andrei Buin, Sjoerd Hoogland, Alexander Rothenberger, Khabiboulakh Katsiev, Yaroslav Losovyj, Xin Zhang, Peter A. Dowben, Omar F. Mohammed, Edward H. Sargent, Osman M. Bakr, *Science*, 2015, 347, 519-522.

108. P. K. Nayak, M. Sendner, B. Wenger, Z. Wang, K. Sharma, A. J. Ramadan, R. Lovrincic, A. Pucci, P. K. Madhu and H. J. Snaith, *J. Am. Chem. Soc.*, 2018, 140, 574-577.

109. O. A. Lozhkina, A. A. Murashkina, V. V. Shilovskikh, Y. V. Kapitonov, V. K. Ryabchuk, A. V. Emeline and T. Miyasaka, *J. Phys. Chem. Lett.*, 2018, 9, 5408-5411.

110. Y. Zhou, Z. J. Yong, K. C. Zhang, B. M. Liu, Z. W. Wang, J. S. Hou, Y. Z. Fang, Y. Zhou, H. T. Sun and B. Song, *J. Phys. Chem. Lett.*, 2016, 7, 2735-2741.

111. M. D. Smith, A. Jaffe, E. R. Dohner, A. M. Lindenberg and H. I. Karunadasa, *Chem. Sci.*, 2017, 8, 4497-4504.

112. M. D. Smith and H. I. Karunadasa, *Acc. Chem. Res.*, 2018, 51, 619-627.

113. F.-P. Zhu, Z.-J. Yong, B.-M. Liu, Y.-M. Chen, Y. Zhou, J.-P. Ma, H.-T. Sun and Y.-Z. Fang, *Opt. Express*, 2017, 25, 33283.

114. N. M. D. a. A. J. N. Prashant V. Kamat, *J. Phys. Chem.*, 1989, 93, 2873-2875.

115. K.-z. Du, X. Wang, Q. Han, Y. Yan and D. B. Mitzi, *ACS Energy Lett.*, 2017, 2, 2486-2490.

116. A. J. Kenyon, *Prog. Quant. Electron.*, 2002, 26, 225–284.

117. T. J. Milstein, D. M. Kroupa and D. R. Gamelin, *Nano Lett.*, 2018, 18, 3792-3799.

118. W. Zheng, P. Huang, Z. Gong, D. Tu, J. Xu, Q. Zou, R. Li, W. You, J. G. Bunzli and X. Chen, *Nat. Commun.*, 2018, 9, 3462.

119. J. T.-W. Wang, Z. Wang, S. Pathak, W. Zhang, D. W. deQuilettes, F. Wisnivesky-Rocca-Rivarola, J. Huang, P. K. Nayak, J. B. Patel, H. A. Mohd Yusof, Y. Vaynzof, R. Zhu, I. Ramirez, J. Zhang, C. Ducati, C. Grovenor, M. B. Johnston, D. S. Ginger, R. J. Nicholas and H. J. Snaith, *Energy Environ. Sci.*, 2016, 9, 2892-2901.

120. Z. K. Wang, M. Li, Y. G. Yang, Y. Hu, H. Ma, X. Y. Gao and L. S. Liao, *Adv. Mater.*, 2016, 28, 6695-6703.

121. Q. Zhang and Y. Yin, *ACS Cent. Sci.*, 2018, 4, 668-679.

122. J. Luo, X. Wang, S. Li, J. Liu, Y. Guo, G. Niu, L. Yao, Y. Fu, L. Gao, Q. Dong, C. Zhao, M. Leng, F. Ma, W. Liang, L. Wang, S. Jin, J. Han, L. Zhang, J. Etheridge, J. Wang, Y. Yan, E. H. Sargent and J. Tang, *Nature*, 2018, 563, 541-545.

123. Z. Tan, J. Li, C. Zhang, Z. Li, Q. Hu, Z. Xiao, T. Kamiya, H. Hosono, G. Niu, E. Lifshitz, Y. Cheng and J. Tang, *Adv. Funct. Mater.*, 2018, 28, 1801131.

TOC Graphic

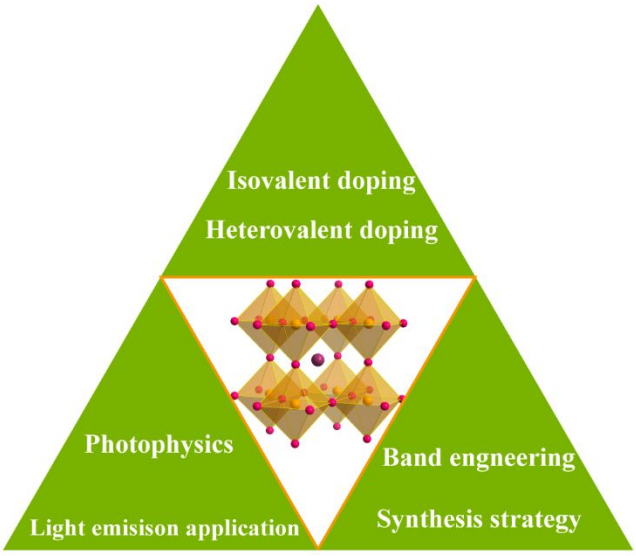
Isovalent doping
Heterovalent doping
Photophysics
Light emisison application
Band engneering
Synthesis strategy